arXiv:1407.3125v2 [astro-ph.HE] 31 Jul 2014

PROPERTIES OF OPTICALLY SELECTED SUPERNOVA REMNANT CANDIDATES IN M33

Jong Hwan Lee and Myung Gyoon Lee

Astronomy Program, Department of Physics and Astronomy, Seoul National University, Seoul 151-747, Korea

leejh@astro.snu.ac.kr, mglee@astro.snu.ac.kr

ABSTRACT

Narrow band images covering strong emission lines are efficient to survey supernova remnants (SNRs) in nearby galaxies. Using the narrow band images provided by the Local Group Galaxy Survey we searched for SNRs in M33. Culling the objects with enhanced [S II]/Hα and round morphology in the continuum-subtracted Hα and [S II] images, we produce a list of 199 sources. Among them 79 are previously unknown. Their progenitor and morphology types were classified. A majority of the sample (170 objects) are likely remnants of core-collapse SNe, and 29 are remnants of Type Ia SNe. The cumulative size distribution of these objects is found to be similar to that of the M31 remnants derived in the similar way. We obtain a power law slope, $\alpha = 2.38 \pm 0.05$. Thus a majority of the sources are considered to be in the Sedov-Taylor phase, consistent with previous findings. The histogram of the emission line ratio ([S II]/Hα) of the remnants has two concentrations at [S II]/H$\alpha \sim 0.55$ and $\sim$0.8, as in M31. Interestingly $L_{\rm X}$ (and $L_{\rm 20cm}$) of the compact center-bright objects are correlated with their optical luminosity. The remnants with X-ray emission have brighter optical surface brightness and smaller diameters than those without X-ray emission.

Subject headings: galaxies: individual (M33) – galaxies: ISM – ISM: supernova remnants

1. INTRODUCTION

Supernova remnants (SNRs) are a unique resource that enables to investigate the final stage of the evolution of massive stars or binary stars interacting with the surrounding interstellar medium (ISM). Studies of individual SNRs in the Milky Way (MW) are important

for understanding the detailed interaction between SNRs and the ISM. However, determining the global properties of the MW SNRs is hard because of uncertain distances to individual remnants and high extinction in the Galactic plane where most of the SNRs are found. Extragalactic SNRs do not suffer from these problems so that they are an ideal target for investigating statistically their global properties and evolution as well as their relationship to the ISM. They provide a clue to understand the star formation history and chemical evolution of galaxies.

Extragalactic SNRs have been identified mostly at three bands: optical, radio and X-ray wavelengths. A majority of the known SNRs in nearby galaxies were detected by optical surveys (Magnier et al. 1995; Matonick & Fesen 1997; Matonick et al. 1997; Pannuti et al. 2002; Blair & Long 2004; Sonbas et al. 2009; Dopita et al. 2010; Franchetti et al. 2012; Blair et al. 2012; Leonidaki et al. 2013). We have been carrying a project to detect SNRs in nearby galaxies. We presented a result of the first target, M31 (Lee et al. 2014, henceforth L14). This paper is the second of the series, presenting the results for M33. M33 is an ideal galaxy for SNR surveys, because it is nearby ($\sim$800 kpc, Lee et al. 2002), relatively face-on ($i = 56^{\circ}$, Regan & Vogel 1994), and a late-type spiral (SA(s)cd) galaxy.

Dodorico et al. (1978) first detected three SNRs using optical images in M33. Subsequent optical studies have increased the number of M33 SNRs to 137 (Long et al. 2010, henceforth L10). Long et al. (1990) showed that the cumulative size distribution (CSD) of 50 SNRs in M33. It follows a power law, having an index $\alpha = 2.1$. They estimated a SN rate to be one per $26 - 300$ yr from the number of SNRs. Gordon et al. (1998, henceforth G98) identified 98 SNRs, of which 53 are previously unknown. They presented a CSD for the 98 SNRs and showed that the Sedov-Taylor (ST) expansion model is a better fit for the distribution than the free expansion model. The ST expansion model is used to derive a SN rate in M33 to be one SN every 360 yr. However, they used narrow images obtained under poor seeing ranging from $2''$ to $2''.4$ (which corresponds to 8-10 pc at a distance of M33). They could not measure the accurate size of SNRs and could not distinguish SNRs on the outskirts of SF regions.

L10 presented a list of 137 SNRs derived from two emission-line surveys using Local Group Galaxy Survey (LGGS) data taken at the KPNO 4m telescope (Massey et al. 2006, 2007) and observational data obtained from 0.6 m Burrell Schmidt telescope at KPNO. They showed that 82 of 137 SNRs are matched with X-ray objects derived from the ChASeM33 survey using *Chandra*. However, they missed a significant fraction of SNRs with low optical surface brightness (SB)($< 10^{-16}$ erg cm^{-2} s^{-1} arcsec^{-2}). They mainly discussed X-ray properties of the SNRs in M33. Recently, Asvarov (2014) estimated a SN rate of M33 to be one SN every 140-150 yr, using X-ray data of the M33 SNRs and physical models at various

conditions of the ambient ISM.

Thus we carry out a new optical search of SNRs in M33 utilizing the images taken in the LGGS. Using these data, we find new M33 remnants, especially those with low SB, concentrating on their optical properties.

2. DATA REDUCTION

2.1. Identification Method

We utilized the Hα and [S II] images in the LGGS to find new M33 remnants. The LGGS covered three 36′ square fields of M33. We subtracted continuum sources from the narrow band images using the R-band images. We smoothed the images with better seeing to match the point-spread-function in the image with worse seeing, using IRAF task $psfmatch$. We then scaled and subtracted the resulting continuum images from narrow band images.

We selected the M33 remnants considering three criteria: emission line ratio ([S II]/Hα), the morphological structure, and the absence of blue stars inside the sources, as done for M31 in L14. Details are described in L14. We detected objects with [S II]/H$\alpha > 0.4$ in emission line ratio maps, and selected the objects with round or shell structures in each narrow band image. As a result, we chose 435 sources.

We estimated an integrated emission line ratio (i.e., the ratio of integrated [S II]/Hα fluxes) for individual remnants to select the genuine SNRs among these candidates. We set an approximate circular region to cover the region with [S II]/H$\alpha > 0.4$ in emission line ratio ([S II]/Hα) maps, and carried out aperture photometry of these sources. We determined the value of the local background for individual remnants, using a 100 pc $\times$ 100 pc box region that shows no emission near the SNR candidate. We selected the objects that have integrated [S II]/H$\alpha > 0.4$. In the cases of the objects with $0.4 <$ [S II]/H$\alpha < 0.6$, we examined the existence of blue stars inside the remnants. We excluded the sources embedding blue stars. Then we removed the objects larger than 100 pc, which is too big to be SNRs (Franchetti et al. 2012, L10;). Finally we considered 199 objects as the probable SNRs, including 79 new ones.

L10 provided a catalog of 137 sources based on optical and X-ray data. We examined these objects according to our identification criteria and considered 17 of these objects to be non-SNRs such as H II regions or superbubbles. Of these, seven objects do not appear to have high enough [S II]/Hα to be cataloged as SNR candidates, and they are likely H II regions. Nine objects have sizes with $D > 100$ pc and embed many blue stars inside,

so that we considered them to be superbubbles. L10 also suggested that these objects are possible superbubbles. One object (L10-35) is an oxygen-dominated SNR with little emission in Hα and [S II] (L10). Table 1 lists the 17 objects excluded according to our criteria. Consequently, we confirmed that 120 of the 137 known objects satisfy our identification criteria.

Figure 1 compares (a) L(Hα), (b) D, (c) SB(Hα), and (d) [S II]/Hα of the remnants in this work and L10. Two measurements for each physical quantity of the objects are correlated well. We fit the data with linear least squares fitting, obtaining (a) log L(Hα)(this work) = 0.94($\pm$0.03) $\times$ log L(Hα)(L10) + 2.12($\pm$1.06) erg s^{-1}, (b) D(this work) = 1.05($\pm$0.05) $\times$ D(L10) $-$ 3.11($\pm$1.94) pc, (c) log SB(Hα)(this work) = 1.20($\pm$0.10) $\times$ log SB(Hα)(L10) $-$ 0.11($\pm$0.07) erg cm^{-2} s^{-1} arcsec^{-2}, and (d) [S II]/Hα (this work) = 1.19($\pm$0.06) $\times$ [S II]/Hα (L10)+ 3.07($\pm$0.89).

We estimated the diameters of the circles covering the region with [S II]/Hα $>$ 0.4 in emission line ([S II]/Hα) images. In the cases of objects with partial shells, we determined their sizes on the basis of the visible portion of the shells. The errors in measuring the sizes are about 0.5$''$ for small objects (D = 10 $\sim$ 50 pc) and about 1$''$ for larger objects (D $>$ 50 pc). L10 determined elliptical regions that best traced optical shells of remnants, and they defined the geometric mean of the major and minor axes of above ellipses as sizes of the sources. They expanded slightly in a few cases to embrace X-ray emission that is apparently associated with the SNR. The errors in their measuring the diameter are 0.5 $-$ 1$''$ for well-defined objects. In Figure 1(b), we compared the diameters of the remnants in this work and L10. They agree well in general. About 10 objects show differences larger than 10 pc. We checked the images of these objects, and confirmed that our measurements are reasonable. The mean difference (D = 10 $\sim$ 40 pc) is derived to be 1.7 pc, showing that our measurements are on average slightly larger than L10's.

2.2. Classification Schemes for Progenitor Type and Morphological Type

We applied the classification schemes for the progenitor type and the morphological type to the M33 SNR sample, as done for M31 in L14. The progenitor types are Type Ia SNRs and core-collapse (CC) SNRs. Details are described in L14. CC SNe are formed by high mass progenitors undergoing core collapse, while Type Ia SNe are formed by white dwarfs in binary systems. The former are typically located in star forming regions, while the latter can be found anywhere in a galaxy, regardless of their host galaxy types. Thus, some previous studies examined the properties of stellar populations around SNRs to identify the nature of their SN progenitors (Chu & Kennicutt 1988; Badenes et al. 2009; Franchetti et al. 2012;

Jennings et al. 2012). An existence of massive stars around an SNR candidate suggests that the remnant may result from a CC SN, while the absence of nearby massive stars suggests that it may be originated from a Type Ia SN. We selected the blue stars with $B - V < 0.0$ and $V < 22.0$ mag ($M_V < -2.5$ mag) from the photometric catalog given by Massey et al. (2006). Then we derived the number of OB stars in the surrounding region within 100 pc for individual remnants, N(OB), following L14. Gvaramadze et al. (2010) showed that some massive runaway stars have been detected at distances of about 100 pc from the center of star clusters in the Large Magellanic Cloud (LMC). Therefore the existence of OB stars within 100 pc from the center an SNR indicates that its progenitor might have been a massive star. We adopted this distance as a boundary to count OB stars for progenitor classification.

Known SNRs have various morphological features: a discrete shell, a filled-center nebula or a diffuse nebula. All the SNR samples in M33 show resolved morphological structure at the resolution of Hα images we use. Even in relatively confused regions on the outskirts of H II regions and SF regions the objects are resolved well. Thus we classified 199 sources in M33 according to their shape as well as environments. Table 2 summarizes our criteria used for the classification. Figure 2 displays some examples of the remnants for individual morphological categories. The majority of A2-class remnants have brighter SB than other types, as shown in Figures 3(a) and (b). The majority of B2-class remnants are embedded in SF regions. Their SB is brighter compared with the other B-class objects, as displayed in Figures 3(c) and (d).

3. RESULTS

3.1. A List of M33 Remnants

By applying the SNR search method described in the previous section, we detected a total of 199 sources. Among these there are 79 new objects detected in this work and 120 known ones in the catalogs of previous studies (G98 and L10). Table 3 presents a list of the 199 sources. In the table the columns give the ID number, the coordinates in right ascension and declination (J2000.0), L, D, [S II]/Hα, morphological types, N(OB), and progenitor types. The last column in Table 3 gives the identification matched with the catalog of L10.

Of the sample, 170 objects result more likely from CC SNe, with the remainder to be from Type Ia SNe. M33 has flocculent spiral arms so that a significant fraction of its disk is occupied by star forming regions. Therefore the Type Ia remnants located in the disk are likely to be classified as the CC remnants according to our classification criteria. Then the 170 sources classified as CC would be an overestimate. If the number density

of the Type Ia remnants is uniform, about 10% of the CC remnants may be the Type Ia remnants. There are a few results for the relative ratio of two categories of remnants (Chu & Kennicutt 1988; Franchetti et al. 2012; L14). According to the study of 32 objects in the LMC by Chu & Kennicutt (1988) more than 60% of them are CC remnants. Franchetti et al. (2012) and L14 also inspected the stellar population around remnants in M101 and M31, respectively. They showed that ∼25% (9 of 34) and ∼27% (42 of 156) are more likely Type Ia remnants, respectively. A fraction (∼17%) of the Type Ia SNR remnants for M33 in this work is smaller than those for M101 and M31.

The majority of the objects with A-class and B-class are CC SNRs (∼85% for each). In the cases of the A3-class (∼31%) and B3-class (∼39%) objects, the Type Ia proportions are high, compared with those of objects of different morphological categories. L14 showed ∼85% of M31 remnants are classified as shell remnants and ∼15% are center-bright remnants. The majority (∼90%) of the M33 remnants are also shell remnants. It is noted that the proportions of the shell remnants and center-bright remnants in the MW at radio wavelengths are 78% and 4%, while the rest is composite type remnants (Green 2009).

3.2. Spatial Distribution

Massive stars (which explode as CC SNe) would tend to be found near SF regions such as H II regions, molecular clouds, and spiral arms, while evolved, lower mass stars (which explode as Type Ia SNe) are expected to be distributed in a more random manner across the plane of a galaxy's disk. Below we examined the distributions of remnants relative to spiral arms as well as the radial distributions of their number density. The positions of the M33 remnants are displayed in Figure 4. The background image (*Sptizer* 24 μm) exhibits the SF regions along the arms. The CC remnants are mainly distributed along the spiral arms. In contrast the majority of the Type Ia remnants are located in the outer part of M33.

The radial number density profile for the M33 remnants is seen in Figure 5. We derived deprojected galactocentric distance (R) adopting the position angle, 22.5° (Paturel et al. 2003) and the inclination angle, 56° (Regan & Vogel 1994). The radial number density profile of all the objects decreases slightly outward with an abrupt break near $R = 4$ kpc. Discernible concentrations are seen at $R \sim 2$ kpc and ∼3.5 kpc, and a much weaker concentration at $R \sim 5$ kpc. The histogram of the A-class remnants shows discernible concentrations at the $R \sim 2$ kpc and ∼3.5 kpc, and the number density decreases slightly outward. On the other hand, the distribution of the B-class remnants decreases more smoothly.

We investigated the radial variation in physical properties of all the remnants in Figure

6: (a) $L(\mathrm{H}\alpha)$ and (b) $L([\mathrm{S\ II}])$, (c) D, (d) $SB(\mathrm{H}\alpha)$ and (e) $SB([\mathrm{S\ II}])$. The $L(\mathrm{H}\alpha)$ and $L([\mathrm{S\ II}])$ of the objects change little at $R < 3.5$ kpc. In the outer region ($R > 3.5$ kpc), $L(\mathrm{H}\alpha)$ and $L([\mathrm{S\ II}])$ of the objects decrease slightly outward. In the same range of R, D increases from 40 pc to 50 pc. Thus, the radial gradients of $SB(\mathrm{H}\alpha)$ and $SB([\mathrm{S\ II}])$ are seen in Figures 6 (d) and (e). This might be caused by the selection bias in our SNR survey. We could find the remnants with more large D and lower SB easily in the outer region of a galaxy.

3.3. Size Distribution

The evolution of SNRs has been a subject of many theoretical studies (Woltjer 1972; Blondin et al. 1998; Truelove & McKee 1999). Some previous studies tried to explain observation data in theoretical aspects (Mathewson et al. 1983; Green 1984; Badenes et al. 2010, henceforth B10; Dopita et al. 2010). Their evolution is described in terms of age. However, it is hard to determine observationally the age of the SNRs. Thus their sizes are used as a proxy for age. The differential size distributions of the M33 remnants are shown in Figure 7(a). Their diameters range from 10 pc to 100 pc. The histogram shows a noticeable concentration at $D \sim 45$ pc with a broad wing toward the large size. A discernible concentration at the same value is seen at the histogram of the CC remnants. On the other hand, no distinguishable concentration is shown at the histogram of the Type Ia remnants. The majority of the objects smaller than $D = 30$ pc are the CC remnants. The mean diameter of the Type Ia remnants is larger than that of the CC remnants. This means that a majority of the CC remnants may lie on denser ambient ISM than the Type Ia remnants.

The CSD of SNRs in a galaxy is useful for studying their evolutionary phases. Their evolution is generally described by the three phase model: the free expansion phase, the ST phase, and the radiative phase (Woltjer 1972; McKee & Ostriker 1977; Dopita & Sutherland 2003; Draine 2011). It is considered that the shapes of the CSD are different, depending on the evolution phase. If the SN rate in a galaxy is constant, the CSD of SNRs becomes steeper as SNRs evolve. During the free expansion phase, it will increase linearly, $N(< D) \propto D$. The power law index will be 2.5 for the ST phase, and that will be 3.5 for the radiative phase. Thus, a study of the CSD of SNRs in a galaxy is important to understand the evolution of SNRs. The transition sizes between these three phases are supposed to depend on several parameters including the density of surrounding ISM, mass of ejected material, and energy released by SNe (Blondin et al. 1998; Truelove & McKee 1999). The transition radius from free expansion phase to ST phase ranges from 1 to 10 pc, and that from ST to radiative phase is about 25 pc.

The CSD of the M33 remnants is seen in Figure 7(b). It follows a power law form ($N(< D) \propto D^{\alpha}$). The power law index is $\alpha = 2.38 \pm 0.05$ ($D = 17 \sim 50$ pc). The majority of the remnants are considered to be in the ST phase. Their number decreases abruptly at $D = 17$ pc as the size of the objects decreases. There are only a few sources that have sizes of $D = 10 \sim 17$ pc. The slope of the CSD of SNRs at $D > 50$ pc is flatter compared with that of smaller SNRs. This indicates two possibilities. First, the flatter slope may be due to incompleteness. We might have missed a significant number of the SNRs, that have large D and low SB in the inner regions of the galaxy. Second, this may correspond to the transition stage from the ST phase to the radiative phase. B10 suggested that the majority of the objects are in the ST phase, and that they rapidly fade away below detection limit once they transit to the radiative phase. The slope for the CC remnants is $\alpha = 2.27 \pm 0.05$ ($D = 17 \sim 50$ pc), but that for the Type Ia remnants is $\alpha = 3.26 \pm 0.12$ ($D = 40 \sim 60$ pc).

In Figures 8(a) and (b), we plot the size histograms of the objects with different morphological categories. The histogram of the A-class remnants shows two concentrations at $D \sim 40$ pc and ∼60 pc, whereas that of the B-class remnants shows a broad concentration at $D \sim 50$ pc. The diameter of the A-class remnants is, on average, $D \sim 45$ pc, which is smaller than that of the B-class remnants, $D \sim 54$ pc. In Figure 8(b), the CSDs of the A-class and B-class remnants have close slopes up to 50 pc. The slopes for the A-class and B-class remnants are $\alpha = 2.44 \pm 0.07$ ($D = 17 \sim 50$ pc) and $\alpha = 2.61 \pm 0.08$ for the same range, respectively. This means that the size evolution of SNRs may not depend on their morphological category.

3.4. [S II]/Hα Distribution

We derived the emission line ratio ([S II]/Hα) to identify the SNR candidates. Objects with [S II]/H$\alpha > 0.4$ were considered as SNRs in our survey. The histograms of emission line ratio ([S II]/Hα) for the sources with different progenitor categories are shown in Figure 9(a). All the objects have [S II]/Hα of 0.4 – 1.2, and their distribution is bimodal, with concentrations at [S II]/H$\alpha \sim 0.55$ and ∼0.8. The histograms for different morphological categories in Figures 9(b) and (c) are roughly divided into two sets at the boundary of [S II]/H$\alpha \sim 0.7$. Most of the A1-class, A2-class, B1-class, and B3-class remnants have elevated [S II]/Hα, whereas most of the A3-class and B2-class remnants have low [S II]/Hα. The A3-class remnants have low SB and smooth shapes. One may suggest that they should be diffuse ionized gas with large D and low SB. Because their mean diameter is $D \sim 50$ pc, we consider the objects to be bona-fide SNRs. The B2-class remnants with high L(Hα) and low [S II]/H$\alpha$are located in SF regions.

3.5. $L - D$ Relation and $SB - D$ Relation

We examined the relations among L, D, and SB of all, Type Ia, and CC remnants in M33. We inspected the relation between L and D of the remnants in Figures 10(a) and (b). Weak correlations between D and L(Hα) (and L([S II])) of all the objects are found. On the other hand, there are better correlations for the Type Ia remnants. We derived from fitting, $L \propto D^{1.78\pm0.29}$ and $L \propto D^{1.83\pm0.33}$ in Hα and [S II], respectively.

The relation between SB and D for the Type Ia and CC remnants in M33 is seen in Figures 10(c) and (d). Weak correlations are found between SB(Hα) (and SB([S II])) and D of all the objects. The Type Ia remnants show better correlations between two parameters than the CC remnants. For the Type Ia remnants, the slopes for SB and D relation in Hα and [S II] are $\beta = -1.62 \pm 0.39$ and $\beta = -1.81 \pm 0.53$, respectively.

4. DISCUSSION

4.1. Comparison with Previous Studies of SNR Candidates in M33

There are several previous studies of M33 SNRs using optical images (Dodorico et al. 1978; Long et al. 1990; G98; L10). The number of known M33 SNRs detected in these studies is 137. In this work we added 79 new ones, which have mostly low SB. We excluded 17 among the 137 known objects as mentioned in Section 2.1. These excluded objects are probably H II regions or superbubbles. In Figure 11 we display the positions of the 79 new objects and the 120 known objects in M33. Previously known sources are mainly concentrated in the inner part of M33, whereas the majority of the new ones are located in the outer part. A majority of the new objects are considered to be relatively evolved sources with low SB at optical wavelengths, so that they are probably too faint to be detected in the previous X-ray surveys.

Figure 12 displays the histograms of L(Hα), L([S II]), SB(Hα), SB([S II]), D, and [S II]/Hα for the known SNR candidates and new ones in M33. The new objects have averagely fainter L, lower SB, and larger D than the known ones. The known objects have [S II]/Hα values ranging from 0.4 to 1.2, with two concentrations at [S II]/H$\alpha \sim 0.55$ and $\sim$0.85. The new ones have close [S II]/Hα values, but with a noticeable concentration at [S II]/H$\alpha \sim 0.5$. The ratio of the number of the known objects to that of the new ones is lower for low [S II]/Hα (< 0.7), than for elevated [S II]/Hα (> 0.7). A small number of the new objects with large D are likely diffuse ionized gas. However, it is hard to distinguish bona-fide SNRs from diffuse ionized gas using only narrow band images.

Figure 13 compares the CSD of the M33 remnants in this work with those in the previous studies (G98 and L10). G98 presented the CSD of 98 remnants and showed that it follows a power law with $\alpha \sim 2.5$. They suggested that the majority of the objects are considered to be in the ST phase. In Figure 13(a), the slope of the CSD obtained from the G98 sample is $\alpha = 2.72 \pm 0.14$ ($D = 13 \sim 33$ pc). The CSD obtained from the L10 sample is shown in Figure 13(b). It follows a double power law with indices $\alpha = 2.82 \pm 0.04$ ($D = 9 \sim 21$ pc) and $\alpha = 1.60 \pm 0.03$ ($D = 21 \sim 50$ pc). Figure 13(c) displays the CSD of the remnants in this work. It follows a power law, and the power index is $\alpha = 2.38 \pm 0.05$ ($D = 17 \sim 50$ pc). If we adopt the same diameter ranges, $D = 19 \sim 36$ pc, for comparison, we obtain $\alpha = 2.23 \pm 0.08$ for this work, $\alpha = 2.24 \pm 0.13$ for the G98 sample, and $\alpha = 1.62 \pm 0.07$ for the L10 sample. Thus the value of the power index for our sample is very close to that of G98, but is much larger than that of L10. The reason for the discrepancy in slope between this work and L10's is considered to be due to the difference in the size measurement. Our measurement is on average slightly larger than L10's, as described in Section 2.1. In conclusion, the majority of the M33 remnants are considered to be in the ST phase, consistent with previous studies (Long et al. 1990; G98).

4.2. Comparison of SNR Candidates in M33 and M31

The two spiral members of the Local Group galaxies, M31 and M33, have been the target of many observational studies to investigate the physical properties of these neighbouring systems. M31 and M33 are the nearest early-type (Sb) and late-type (Scd) spiral galaxies, respectively. Therefore, they may experience different star formation activities and have different ISM conditions. One might expect that there is a difference in the distributions of physical properties of SNRs in two galaxies.

We compared the physical properties of the M33 remnants in this work with those of the M31 remnants studied using the similar methods by L14. In Figures 14(a) and (b) we compare the histograms of $L(\mathrm{H}\alpha)$ and $L([\mathrm{S\ II}])$, respectively. The SNR detection limits for both M31 and M33 are found to be close. The histograms of $SB(\mathrm{H}\alpha)$ and $SB([\mathrm{S\ II}])$ have similar ranges as plotted in Figures 14(c) and (d). Figure 14(e) compare the differential size distributions of the remnants in two galaxies. The histogram of the objects in M33 has a concentration at $D \sim 45$ pc, close to that of the sources in M31. Figure 14(f) plots the histogram of emission line ratio ([S II]/Hα) of the remnants in M33 and M31. The histogram of the sources in M33 is bimodal, with two concentrations at [S II]/H$\alpha \sim 0.55$ and $\sim$0.8, and that of objects in M31 is also nearly bimodal, having two concentrations at [S II]/H$\alpha \sim 0.4$ and $\sim$0.9. In conclusion, there is little difference in the distributions of physical properties

between the M31 and M33 SNR candidates.

4.3. Comparison of CSDs of the SNRs

The CSDs of SNRs can be often described by the power law (Mathewson et al. 1983; Mills et al. 1984; Green 1984; Hughes & Helfand 1984; Long et al. 1990; Dopita et al. 2010). The CSDs of both the MW SNRs and SNRs in the Magellanic Clouds (MCs) were represented well by a power law index $\alpha \sim 1$ (Mathewson et al. 1983; Mills et al. 1984; Hughes & Helfand 1984), while the M33 remnants follow a power law, having an index $\alpha \sim 2.5$ (G98). L14 presented the CSD of M31 remnants. It follows a power law, having an index $\alpha \sim 2.5$. The CSD is taken as evidence that the majority of the remnants in the MW and the MCs are likely to be in the free expansion phase, while the majority of the objects in the M31 and M33 are considered to be in the ST phase.

In Figure 15, the CSD of the M33 remnants is compared with those for the MCs, the MW, and M31. The CSDs for individual galaxies follow a power law. Table 4 presented the different power law indices among galaxies. Figure 15(a) displays the CSD of the M33 remnants. The power law index is $\alpha = 2.38 \pm 0.05$ ($D = 17 \sim 50$ pc). In Figure 15(b), we display the CSD of the remnants in the MCs. We derived the power law slopes using the B10 sample. The value for the LMC SNRs is $\alpha = 1.34 \pm 0.04$ ($D = 15 \sim 55$ pc), and that for the SMC SNRs is $\alpha = 1.18 \pm 0.03$ ($D = 25 \sim 50$ pc). These results means that most of the MC SNRs are probably in the free expansion phase. However, it is noted that the shapes of the CSDs of SNRs depend also on selection effect (Mills et al. 1984) and the density distribution of ISM (B10).

Figure 15(c) plots the CSD derived from the catalog of 274 MW SNRs (Pavlović et al. 2013). They estimated the sizes of most SNRs using the relation between radio SB and D derived from SNRs with known distances. Thus the size estimates of these SNRs have large uncertainties. The majority of the MW SNRs have diameters with $D = 15 - 30$ pc. The slope for the size distribution is $\alpha = 3.60 \pm 0.06$ ($D = 15 \sim 30$ pc). This is much steeper than the value for M33, indicating that most of the MW SNRs are likely to be in the radiative phase. The CSD of the objects in M31 obtained from L14 is seen in Figure 15(d). They presents the diameters of the 156 sources in M31 detected in the LGGS data. The slope of the CSD of these SNRs is derived to be $\alpha = 2.53 \pm 0.04$ (D= 17 $\sim$ 50 pc). This value is very close to that for the objects in M33.

4.4. Multiwavelength Properties of Remnants

Inspecting the properties of SNRs in multiwavelength images is useful for understanding their nature and evolution. Some previous studies for extragalactic SNRs showed weak or little correlations among X-ray, radio, and optical properties of SNRs (Pannuti et al. 2007; L10; Leonidaki et al. 2013). On the other hand, a good correlation between $L_{\rm X}$ and $L({\rm H}\alpha)$ for the center-bright remnants in M31 were found by L14. Here we discuss any correlations between X-ray (radio) and optical properties of the M33 remnants.

First, the optical properties of the M33 remnants are compared with their property at X-ray wavelengths. L10 detected 82 X-ray bright sources among the 137 optically selected samples using *Chandra* data from the ChASeM33 survey. Of 199 sources detected in this work, 78 are matched with L10 catalog. Much larger proportions of the remnants with complete shells ($\sim$51% and $\sim$95% for A1-clsss and A2-class remnants, respectively) are found at the X-ray wavelengths. In Figures 16(a) and (b), $L({\rm H}\alpha)$ and $L([{\rm S\ II}])$ of the matched sources are compared with $L_{\rm X}$, respectively. All the matched sources with an exception are brighter at optical wavelengths than at X-ray wavelengths. Weak correlations between the optical luminosity ($L_{\rm opt}$) and $L_{\rm X}$ are found for all the matched objects. In the cases of the A2-class remnants, we calculated the linear Pearson correlation coefficients in Hα and [S II], obtaining 0.66 and 0.69 (corresponding probabilities for given numbers of the sample are $\sim$99% for each). They show that the two sets of quantities have strong correlations.

In contrast, there are little correlation between $L_{\rm opt}$ and $L_{\rm X}$ of the B-class SNRs. The correlation difference between the A-class remnants and the B-class remnants is considered to be related with the distribution of the ambient ISM. Pannuti et al. (2007) pointed out, based on simple emissivity models, that $L_{\rm opt}$ and $L_{\rm X}$ of SNRs might increase with increasing density of the ambient ISM. They expected a good correlation between $L_{\rm opt}$ and $L_{\rm X}$ of SNRs, if the ambient ISM is uniform. The correlation between $L_{\rm opt}$ and $L_{\rm X}$ of the A-class remnants is stronger than that of the B-class remnants in M33. This means that the ISM around the A-class remnants is more uniform than that around the B-class remnants.

Figures 16(c) and (d) show $L_{\rm X}$ versus $SB({\rm H}\alpha)$ and $SB([{\rm S\ II}])$, respectively, of the matched sources. There are tight correlations between SB of only the A2-class remnants and $L_{\rm X}$. Correlation coefficients are derived to be 0.63 (and 0.69) in Hα (and [S II]). Thus the two samples are considered to be strongly correlated.

Second, we inspected the correlation between optical and radio properties of the M33 remnants. Gordon et al. (1999) presented a catalog of 186 radio sources obtained from $VLA-WRST$ observations. We found that 43 of the 199 optically selected samples in this work are matched with Gordon et al. (1999) catalog. Higher fractions of the A2-class ($\sim$63%)

and B2-class (∼42%) remnants are detected than other categories at radio wavelengths as well as at optical wavelengths. Figures 17(a) and (b) show comparisons of L(Hα) and L([S II]) of the matched sources with $L_{20\rm cm}$, respectively. Weak correlations between $L_{\rm opt}$ and $L_{20\rm cm}$ for all the matched objects are found, but strong correlations for the A2-class remnants. In Figures 17(c) and (d), we plot $L_{20\rm cm}$ versus SB(Hα) and SB([S II]), respectively, of the matched sources. We found that there are also good correlations between SB(Hα) and $L_{20\rm cm}$.

The histograms of SB(Hα) and SB([S II]) for the objects with X-ray emission, those without X-ray emission, and all the M33 remnants are seen in Figure 18. The majority of the objects with large SB(Hα) (and SB([S II])) have X-ray counterparts. The distributions in Hα and [S II] of the objects with X-ray emission show concentrations at $10^{-15.7}$ erg cm^{-2} s^{-1} arcsec^{-2} and $10^{-15.9}$ erg cm^{-2} s^{-1} arcsec^{-2}, respectively. The majority of the objects with low SB have no X-ray counterparts. The objects with X-ray emission have a nearly flat distribution for $D = 15 - 60$ pc as shown in Figure 19(a). The objects with X-ray emission have a median D of 38 pc, smaller than the value of 50 pc for those without X-ray emission. Figure 19(b) shows that the slope for the objects with X-ray emission is $\alpha = 2.26 \pm 0.2$ ($D = 19 \sim 30$ pc), while that for those without X-ray emission is $\alpha = 2.21 \pm 0.05$. However, the slopes of the CSD of the remnants for $30 < D < 46$ pc are different. The slopes for the objects with X-ray emission is $\alpha = 1.52 \pm 0.02$, much flatter than those without X-ray emission, $\alpha = 4.11 \pm 0.11$.

5. SUMMARY

We presented a survey of SNR candidates in M33 using the [S II]/Hα technique to the optical narrow band images. We expanded the remnant list to 199 objects, of which 79 are new findings. We utilized this catalog to study their optical and X-ray properties. We found that the majority of them are the remnants of CC SNe. Type Ia proportion (∼15%) for M33 is lower than that for M31 (∼27%) (L14). The radial number density profile of the remnants shows two significant concentrations at $R \sim 2$ kpc and ~ 3.5 kpc. For $R > 3.5$ kpc, the sizes of the objects increase, on average, slightly outward. In contrast the mean value of their SB(Hα) (and SB([S II])) decreases. A noticeable concentration is seen at $D \sim 45$ pc in the differential size distribution of the CC remnants. Power law fitting to the CSD of the remnants yielded a value, $\alpha = 2.38 \pm 0.05$ (for the range of $D = 17 - -50$ pc). This value is close to the value from that for the M31 remnants, $\alpha = 2.53 \pm 0.04$ (L14). Thus the majority of the objects in both M33 and M31 are the ST phase. The histogram of the emission line ratio ([S II]/Hα) of the remnants has two concentrations, at [S II]/H$\alpha \sim 0.55$ and ∼0.8. Tight correlations between D and L(Hα) (and L([S II])) for the Type Ia remnants

are found. A significant proportion of the remnants are detected in X-rays for the A1-class and A2-class ($\sim$51% and $\sim$95%, respectively). These sources have mostly large SB, small D, and complete shapes at optical wavelengths. Strong correlations between $L_{\rm X}$(and $L_{\rm 20cm}$) and optical properties are found for the A2-class remnants.

This work was supported by a National Research Foundation of Korea (NRF) grant funded by the Korea Government (MSIP) (No. 2012R1A4A1028713).

REFERENCES

Asvarov, A. I. 2014, A&A, 561, A70

Badenes, C., Harris, J., Zaritsky, D., & Prieto, J. L. 2009, ApJ, 700, 727

Badenes, C., Maoz, D., & Draine, B. T. 2010, MNRAS, 407, 1301 [B10]

Bandiera, R., & Petruk, O. 2010, A&A, 509, A34

Blair, W. P., & Long, K. S. 2004, ApJS, 155, 101

Blair, W. P., Winkler, P. F., & Long, K. S. 2012, ApJS, 203, 8

Blondin, J. M., Wright, E. B., Borkowski, K. J., & Reynolds, S. P. 1998, ApJ, 500, 342

Chu, Y.-H., & Kennicutt, R. C., Jr. 1988, AJ, 96, 1874

Dodorico, S., Benvenuti, P., & Sabbadin, F. 1978, A&A, 63, 63

Dopita, M. A., Blair, W. P., Long, K. S., et al. 2010, ApJ, 710, 964

Dopita, M. A., & Sutherland, R. S. 2003, Astrophysics of the Diffuse Universe (Berlin: Springer)

Draine, B. T. 2011, Physics of the Interstellar and Intergalactic Medium (Princeton, NJ:Princeton Univ. Press), Chapter 39

Franchetti, N. A., Gruendl, R. A., Chu, Y.-H., et al. 2012, AJ, 143, 85

Gordon, S. M., Duric, N., Kirshner, R. P., Goss, W. M., & Viallefond, F. 1999, ApJS, 120, 247

Gordon, S. M., Kirshner, R. P., Long, K. S., et al. 1998, ApJS, 117, 89 [G98]

Green, D. A. 2009, BASI, 37, 45

Green, D. A. 1984, MNRAS, 209, 449

Gvaramadze, V. V., Kroupa, P., & Pflamm-Altenburg, J. 2010, A&A, 519, A33

Hughes, J. P., & Helfand, D. J. 1984, BAAS, 16, 927

Jennings, Z. G., Williams, B. F., Murphy, J. W., et al. 2012, ApJ, 761, 26

Leonidaki, I., Boumis, P., & Zezas, A. 2013, MNRAS, 429, 189

Lee, M. G., Kim, M., Sarajedini, A., Geisler, D., & Gieren, W. 2002, ApJ, 565, 959

Lee, J. H., & Lee, M. G., 2014, ApJ, 786, 130 [L14]

Long, K. S., Blair, W. P., Kirshner, R. P., & Winkler, P. F. 1990, ApJS, 72, 61

Long, K. S., Blair, W. P., Winkler, P. F., et al. 2010, ApJS, 187, 495 [L10]

Long, K. S., Charles, P. A., Blair, W. P., & Gordon, S. M. 1996, ApJ, 466, 750

Magnier, E. A., Prins, S., van Paradijs, J., et al. 1995, A&AS, 114, 215

Massey, P., McNeill, R. T., Olsen, K. A. G., et al. 2007, AJ, 134, 2474

Massey, P., Olsen, K. A. G., Hodge, P. W., et al. 2006, AJ, 131, 2478

Mathewson, D. S., Ford, V. L., Dopita, M. A., et al. 1983, ApJS, 51, 345

Matonick, D. M., & Fesen, R. A. 1997, ApJS, 112, 49

Matonick, D. M., Fesen, R. A., Blair, W. P., & Long, K. S. 1997, ApJS, 113, 333

McKee, C. F., & Ostriker, J. P. 1977, ApJ, 218, 148

Mills, B. Y., Turtle, A. J., Little, A. G., & Durdin, J. M. 1984, AuJPh, 37, 321

Pannuti, T. G., Duric, N., Lacey, C. K., et al. 2002, ApJ, 565, 966

Pannuti, T. G., Schlegel, E. M., & Lacey, C. K. 2007, AJ, 133, 1361

Paturel, G., Petit, C., Prugniel, P., et al. 2003, A&A, 412, 45

Pavlović, M. Z., Urošević, D., Vukotić, B., Arbutina, B., & Göker, Ü. D. 2013, ApJS, 204, 4

Regan, M. W., & Vogel, S. N. 1994, ApJ, 434, 536

Schlafly, E. F., & Finkbeiner, D. P. 2011, ApJ, 737, 103

Sonbas, E., Akyuz, A., & Balman, S. 2009, A&A, 493, 1061

Truelove, J. K., & McKee, C. F. 1999, ApJS, 120, 299

Woltjer, L. 1972, ARA&A, 10, 129

This preprint was prepared with the AAS LaTeX macros v5.2.

Table 1. A List of Previous M33 SNR Candidates Excluded in This Work

Name	R.A.(J2000.0)[a] (Degree)	Decl.(J2000.0)[a] (Degree)	log L(Hα)[b] (erg s^{-1})	log L([S II])[b] (erg s^{-1})	D[c] (pc)	[S II]/Hα	Class.[d]
L10-1	23.1262779	30.462805	37.02	37.01	136	0.98	S
L10-3	23.1772499	30.349541	36.77	36.58	98	0.64	S
L10-12	23.2502728	30.512455	37.49	37.07	62	0.38	H
L10-19	23.2814598	30.714882	36.66	36.21	74	0.35	H
L10-28	23.3278923	30.451220	37.10	36.84	158	0.55	S
L10-35[e]	23.3708439	30.795719	35.52	34.65	18	0.13	
L10-43	23.3974609	30.708994	37.28	36.72	80	0.28	H
L10-50	23.4197102	30.709921	37.06	36.84	100	0.60	S
L10-68	23.4672909	30.942835	36.93	36.65	112	0.52	S
L10-79	23.4922905	30.810335	37.14	36.61	80	0.29	H
L10-98	23.5528698	30.586670	36.61	36.10	62	0.31	H
L10-122	23.6327095	30.944935	36.94	36.87	126	0.85	S
L10-131	23.6745396	30.626440	36.87	36.52	156	0.45	S
L10-132	23.6857471	30.710779	36.39	35.86	50	0.29	H
L10-133	23.7286701	30.688061	36.94	36.48	72	0.35	H
L10-136	23.7550793	30.638155	36.65	36.27	124	0.42	S
L10-137	23.7632504	30.619329	36.61	36.53	124	0.83	S

[a]Measured in the Hα image.

[b]Derived using $L = 4\pi d^2 \times$ flux adopting d = 800 kpc.

[c]Size derived using $1'' = 3.88$ pc.

[d]H:H II regions with [S II]/H$\alpha < 0.4$, and blue stars inside; S: Superbubbles (Larger than $D =$ 100 pc and a number of blue stars inside).

[e]An oxygen-dominated SNR with little emission in Hα and [S II] (L10).

Table 2. Characteristics of M33 SNR Candidates of Different Morphological Categories

Type	Number[a]	L(Hα)	L([S II])	D	[S II]/Hα	Environment	Description
A1	41(5)	Moderate	Moderate	Moderate	High	Isolated	Complete shells
A2	19(0)	High	High	Small	High	Isolated	Center-bright remnants
A3	29(9)	Low	Low	Small	Low	Isolated	Diffuse and extended shells
B1	36(3)	Moderate	Moderate	Moderate	High	Isolated	Partial shells
B2	24(0)	High	High	Moderate	Low	Confused	Bright partial shells
B3	28(11)	Low	Moderate	Large	High	Isolated	Diffuse partial shells
C[b]	21(1)	...	...	...	...	...	...

[a]Values in parentheses represent numbers of Type Ia remnants.

[b]Ambiguous objects, excluding A-class and B-class remnants.

Table 3. A List of M33 SNR Candidates

ID	R.A.(J2000.0)[a] (Degree)	Decl.(J2000.0)[a] (Degree)	log L(Hα)[b] (erg s^{-1})	log L([S II])[b] (erg s^{-1})	D[c] (pc)	[S II]/Hα	Morphology Type	N(OB)[d]	Progenitor Type	Comments
1	23.1074047	30.501122	36.16	36.03	81	0.74	B3	4	CC	
2	23.1160583	30.595718	36.05	36.04	72	0.98	B3	6	CC	
3	23.1306095	30.592470	36.02	35.79	28	0.59	C	18	CC	L10-2
4	23.1473484	30.588837	36.36	36.06	85	0.50	A3	2	CC	
5	23.1548519	30.298412	36.15	35.93	85	0.60	B3	0	Ia	
6	23.1657581	30.465267	35.36	35.33	36	0.93	B3	3	CC	
7	23.1676331	30.272575	35.65	35.37	44	0.52	A3	1	Ia	
8	23.1694889	30.275404	35.36	35.26	42	0.79	A3	1	Ia	
9	23.1705875	30.530849	36.36	36.07	86	0.51	A3	1	Ia	
10	23.1779709	30.605574	36.07	35.76	58	0.49	B	17	CC	

[a]Measured in the Hα image.

[b]Derived using $L = 4\pi d^2 \times$ flux adopting d = 800 kpc.

[c]Size derived using $1'' = 3.88$ pc.

[d]Numbers of OB stars within 100 pc from the center of individual remnants.

(This table is available in its entirety in a machine-readable form in the online journal.
A portion is shown here for guidance regarding its form and content.)

Table 4. Power Law Indices for Cumulative Size Distributions of SNR Candidates in Nearby Galaxies

Galaxies	N	Fitting Range of D	α^*	Phase	Reference	Wavelength
M33	111	$17 \sim 50$ pc	2.38 ± 0.05	ST	This work	Optical (LGGS)
M33	46	$19 \sim 36$ pc	2.23 ± 0.08	ST	This work	Optical (LGGS)
M33	47	$13 \sim 33$ pc	2.72 ± 0.14	ST	G98	Optical
M33	45	$19 \sim 36$ pc	2.24 ± 0.13	ST	G98	Optical
M33	18	$9 \sim 21$ pc	2.82 ± 0.04	...	L10	X-ray, Optical(LGGS)
M33	69	$21 \sim 50$ pc	1.60 ± 0.03	...	L10	X-ray, Optical(LGGS)
M33	40	$19 \sim 36$ pc	1.62 ± 0.07	...	L10	X-ray, Optical(LGGS)
LMC	33	$15 \sim 55$ pc	1.34 ± 0.04	Free expansion	B10	X-ray, Optical, Radio
SMC	11	$25 \sim 50$ pc	1.18 ± 0.03	Free expansion	B10	X-ray, Optical, Radio
MW	111	$15 \sim 30$ pc	3.60 ± 0.06	Radiative	Pavlović et al. (2013)	Radio ($\Sigma - D$ relation)
M31	85	$17 \sim 50$ pc	2.53 ± 0.04	ST	L14	Optical (LGGS)

*We derived the power law indices using the catalogs of remnants in the references.

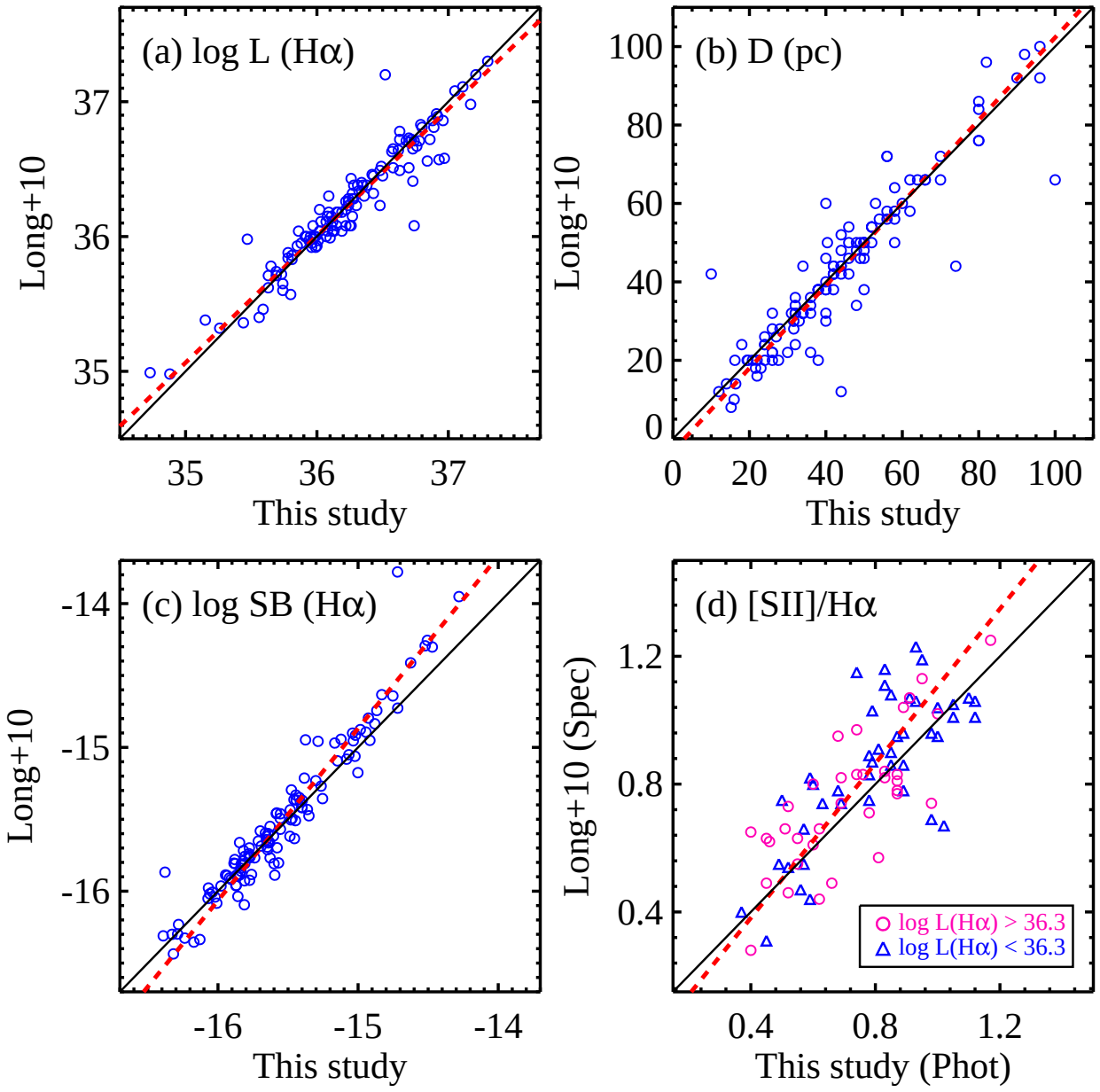

Fig. 1.— Comparison of (a) L(Hα), (b) D, (c) SB(Hα), and (d) [S II]/Hα of M33 remnants in this work and L10. Linear least-squares fit lines (dashed line) are close to the one-to-one relation (solid line): (a) log L(Hα)(this work) = 0.94($\pm$0.03) $\times$ log L(Hα)(L10) + 2.12($\pm$1.06) erg s^{-1}, (b) D(this work) = 1.05($\pm$0.05) $\times$ D(L10) $-$ 3.11($\pm$1.94) pc, (c) log SB(Hα)(this work) = 1.20($\pm$0.10) $\times$ log SB(Hα)(L10) $-$ 0.11($\pm$0.07) erg cm^{-2} s^{-1} arcsec^{-2}, and (d) [S II]/Hα (this work) = 1.19($\pm$0.06) $\times$ [S II]/Hα (L10)+ 3.07($\pm$0.89).

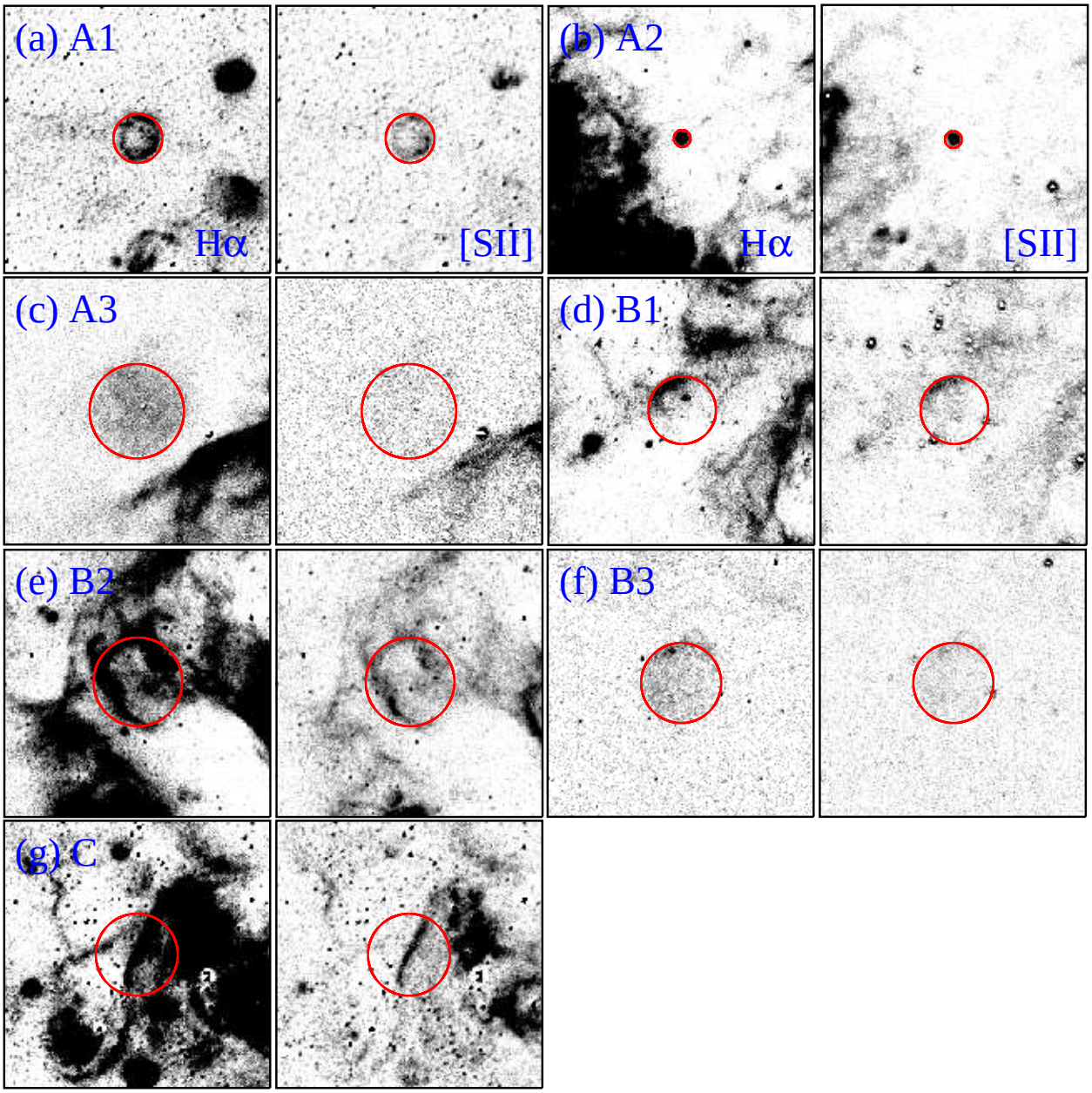

Fig. 2.— Samples of M33 remnants with different morphological categories. Sizes of the objects are marked by circles. An individual image covers 64.″8 × 64.″8 (251 pc × 251 pc). North is up, and east to the left.

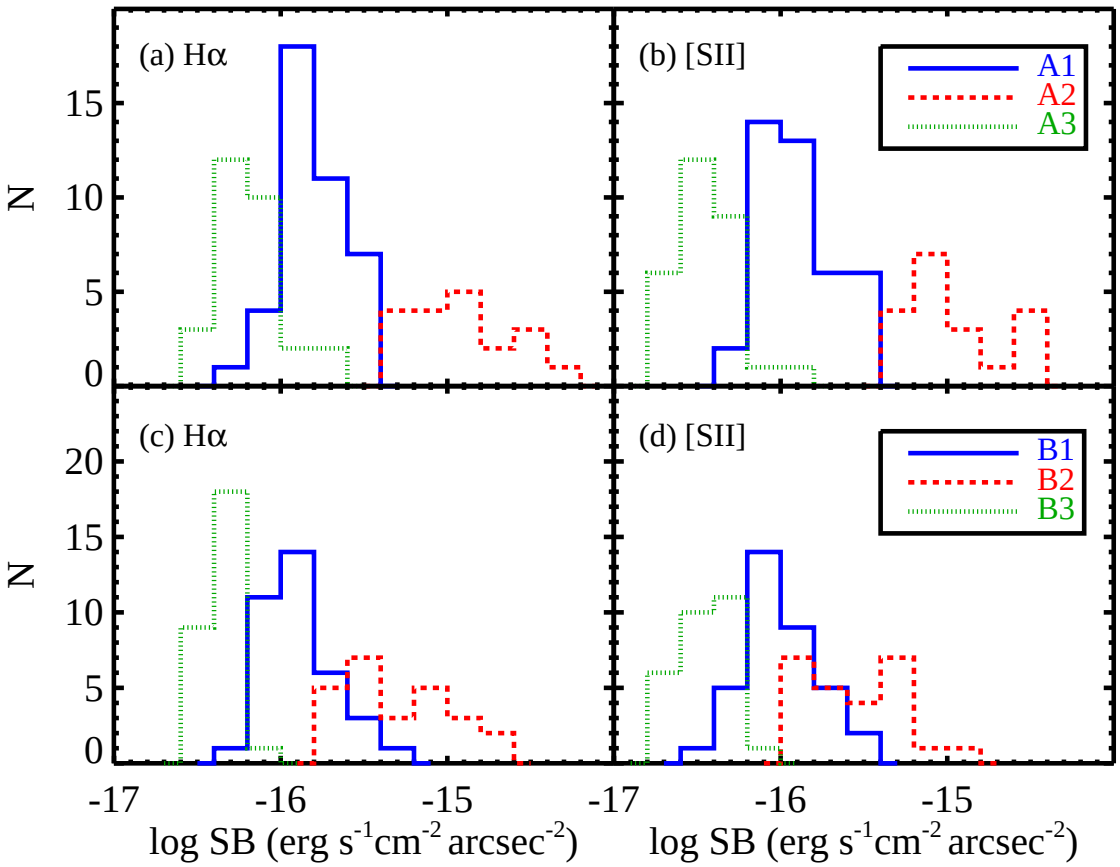

Fig. 3.— Histograms of $SB(\mathrm{H}\alpha)$ (left panel) and $SB([\mathrm{S\ II}])$ (right panel) of M33 remnants with different morphological categories.

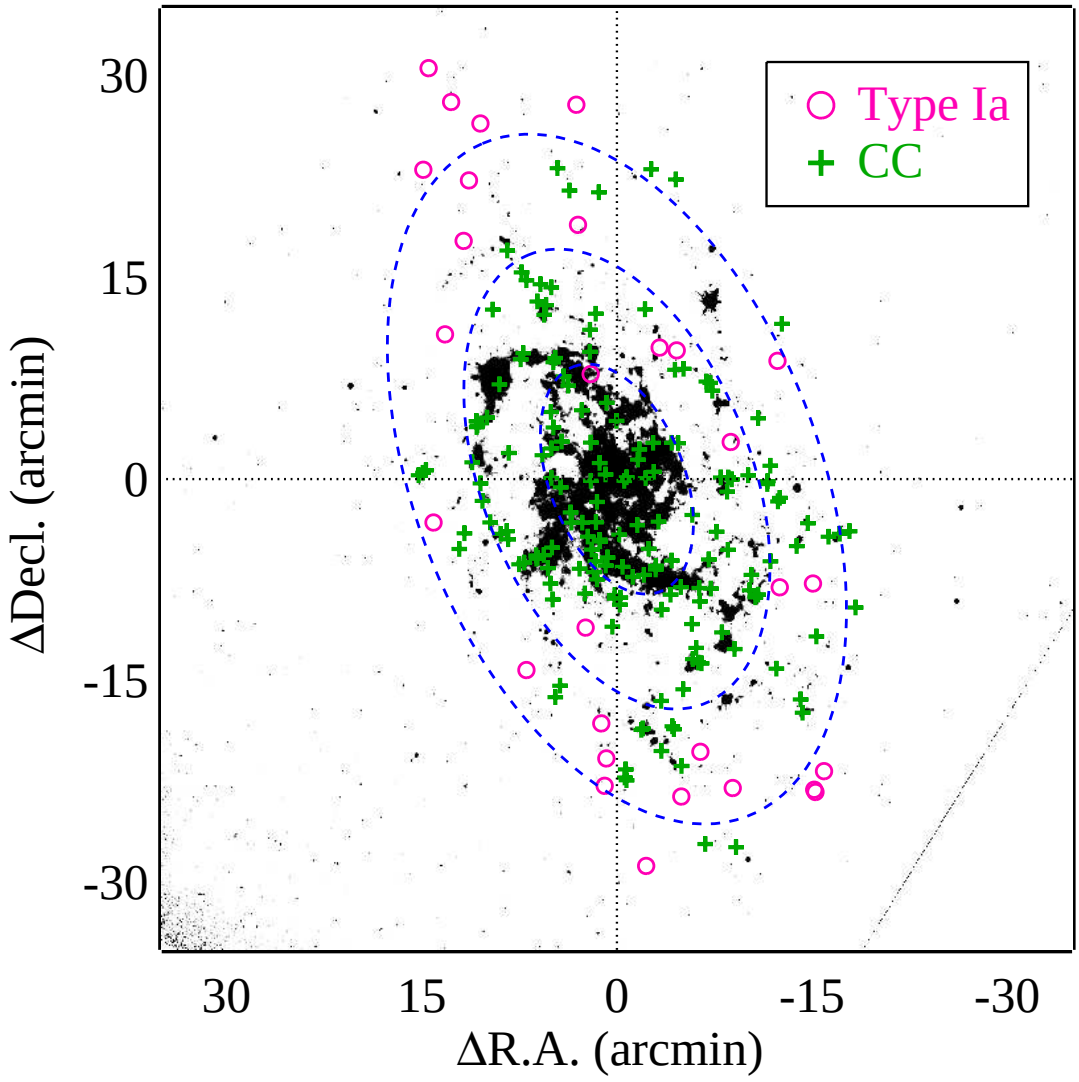

Fig. 4.— Positions of Type Ia and CC remnants in M33 plotted over the gray-scale map of the *Spitzer* MIPS 24 μm image. Dashed line ellipses represent 2, 4, and 6 kpc from the center.

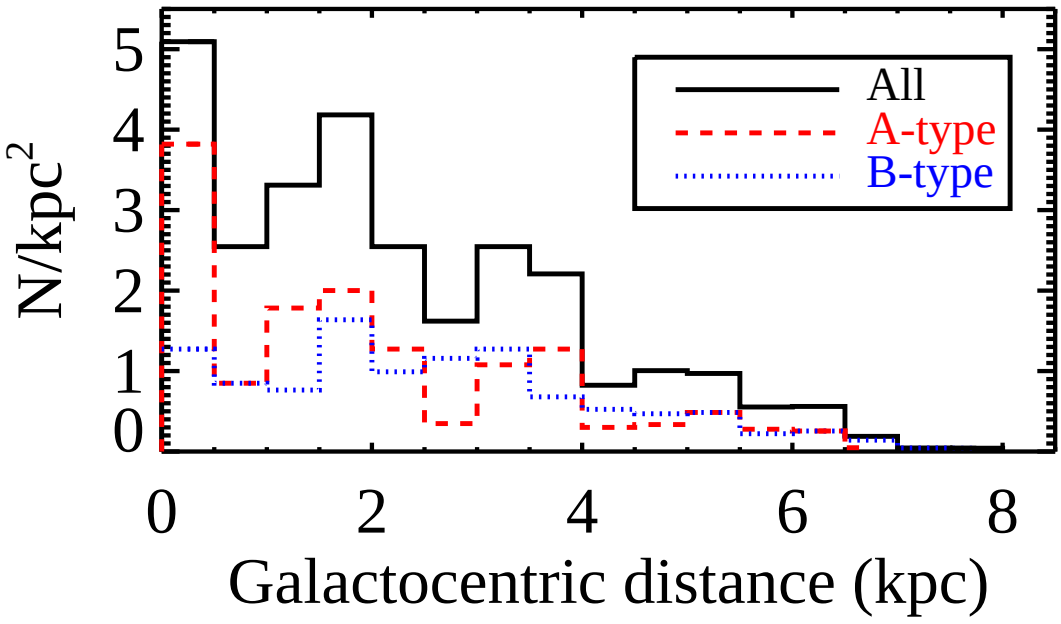

Fig. 5.— Number density versus galactocentric distance of all, A-class, and B-class remnants in M33.

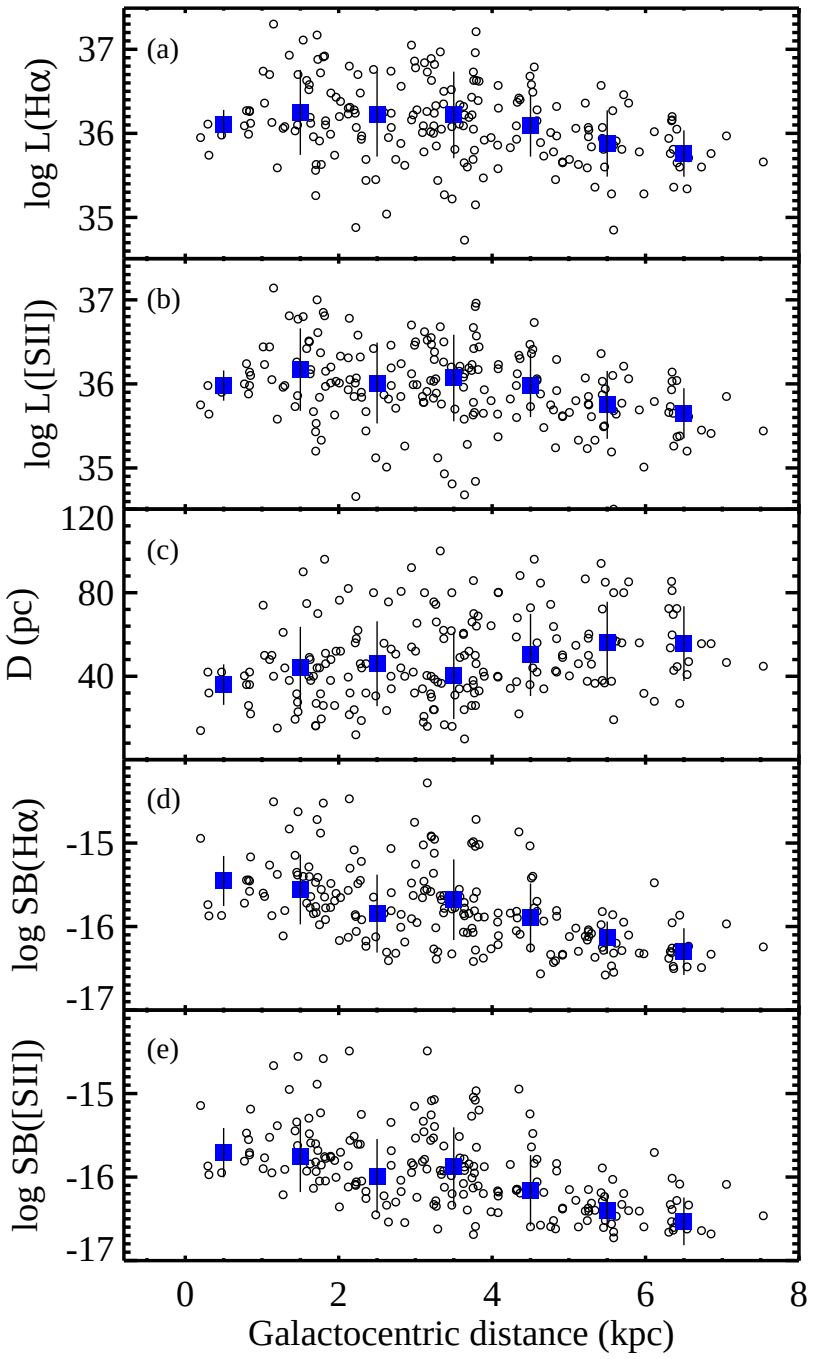

Fig. 6.— Radial distributions of (a) L(Hα) and (b) L([S II]), (c) D, (d) SB(Hα) and (e) SB([S II]), of M33 remnants. Mean values are plotted by square symbols.

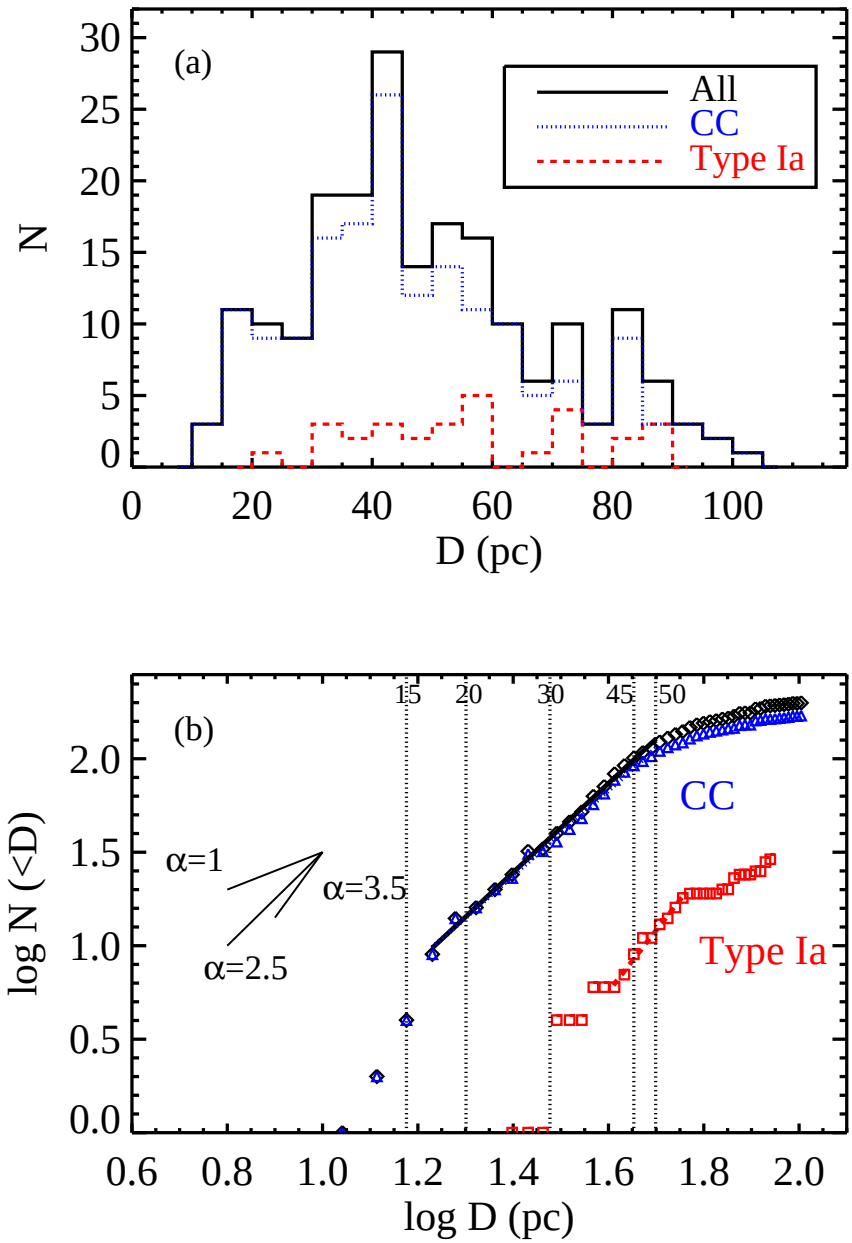

Fig. 7.— (a) Differential and (b) cumulative size distributions of all, CC, and Type Ia remnants in M33.

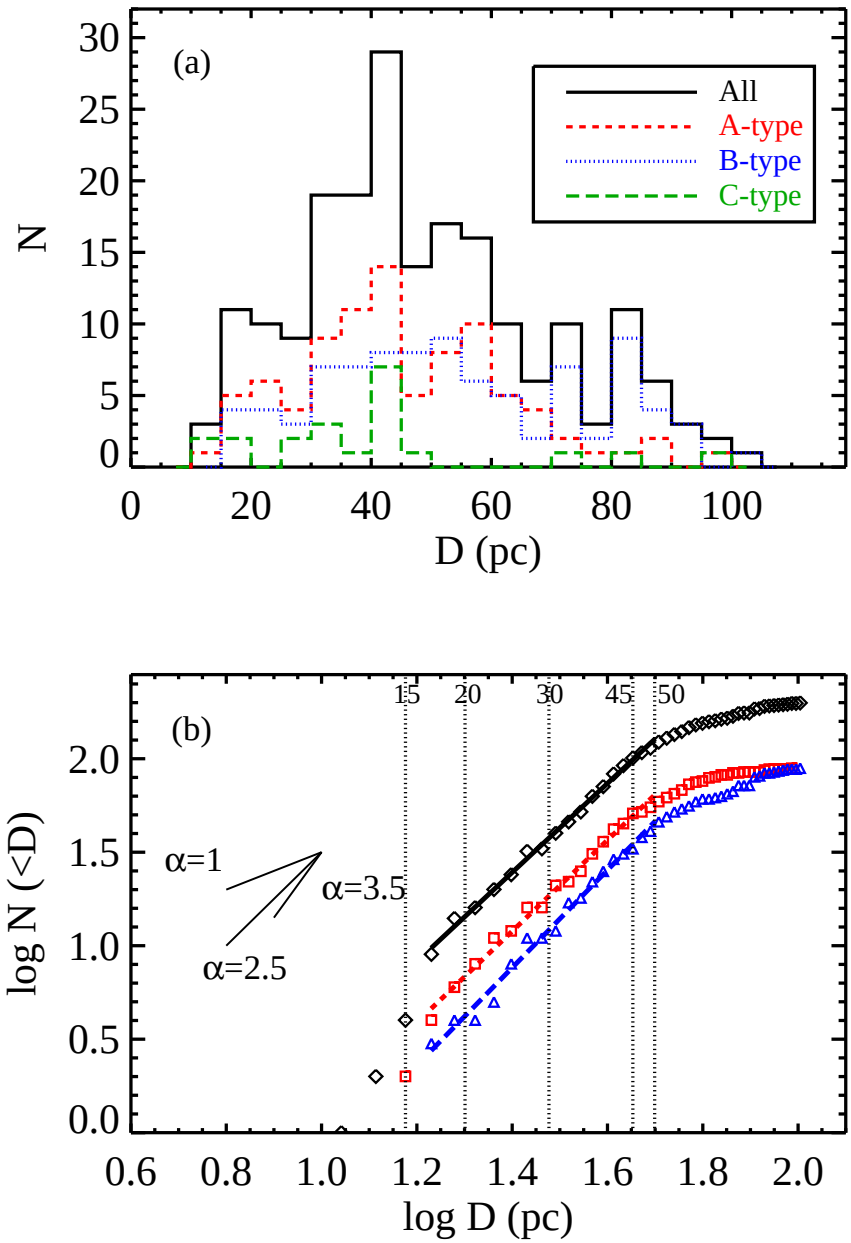

Fig. 8.— (a) Differential and (b) cumulative size distributions of all, A-class, B-class, and C-class remnants in M33.

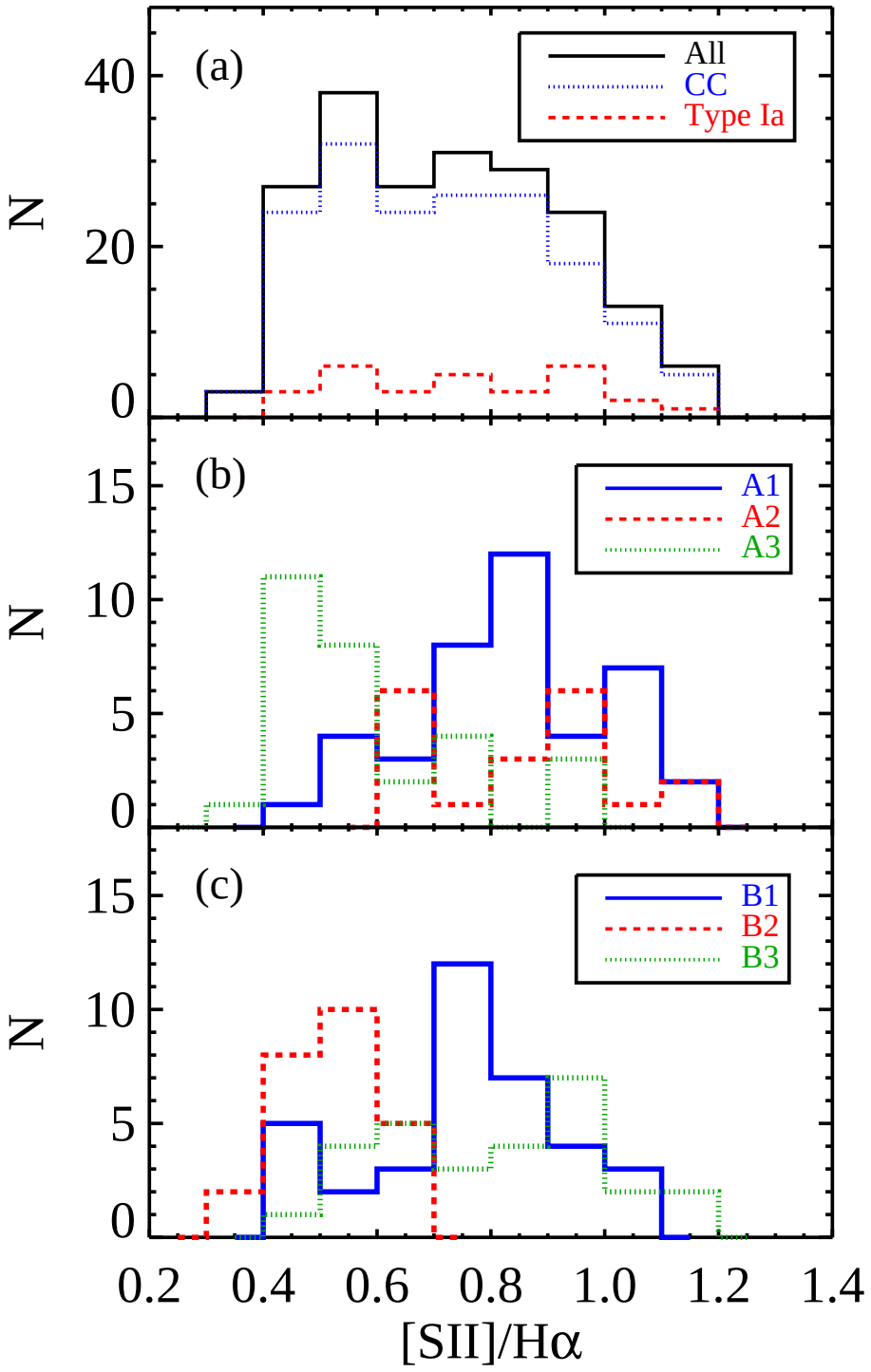

Fig. 9.— Histograms of the [S II]/Hα flux ratio of M33 remnants: (a) different progenitor categories, (b) and (c) different morphological categories.

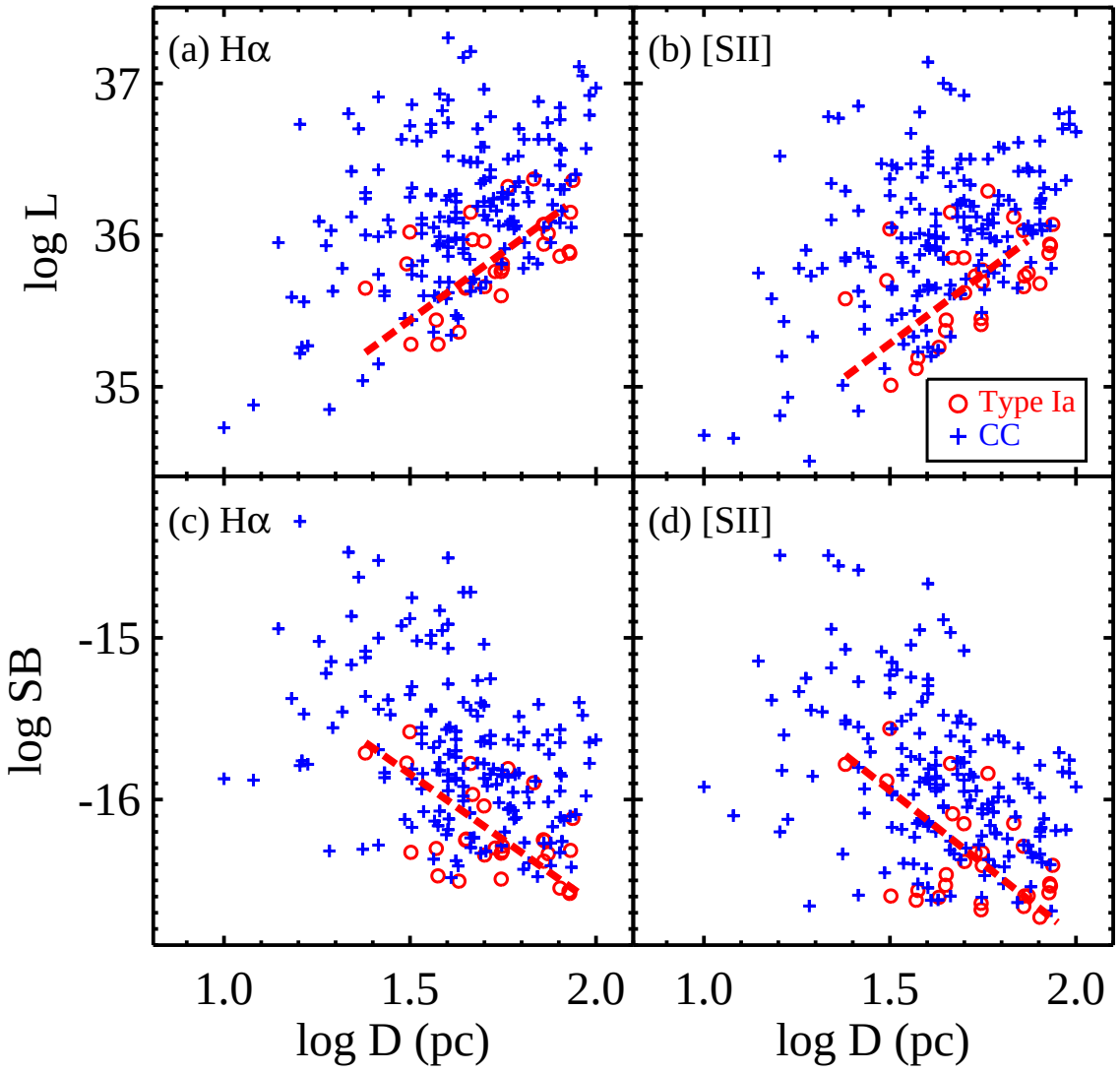

Fig. 10.— Upper panel: the relations between L versus D and lower panel : the relations between SB versus D for Type Ia and CC remnants in M33. Dashed lines indicate linear least-squares fits.

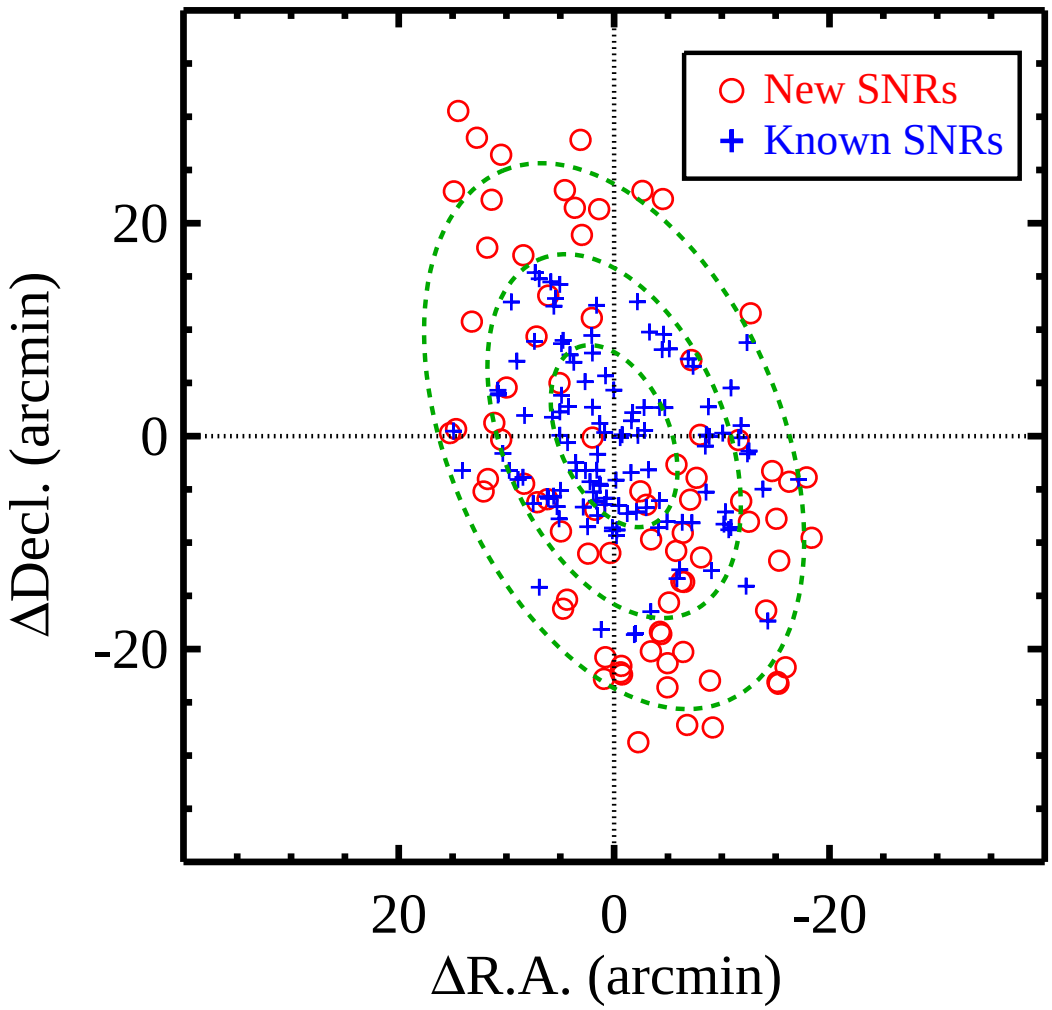

Fig. 11.— Positions of newly found remnants and known ones in M33. Dashed line ellipses represent 2, 4, and 6 kpc from the center.

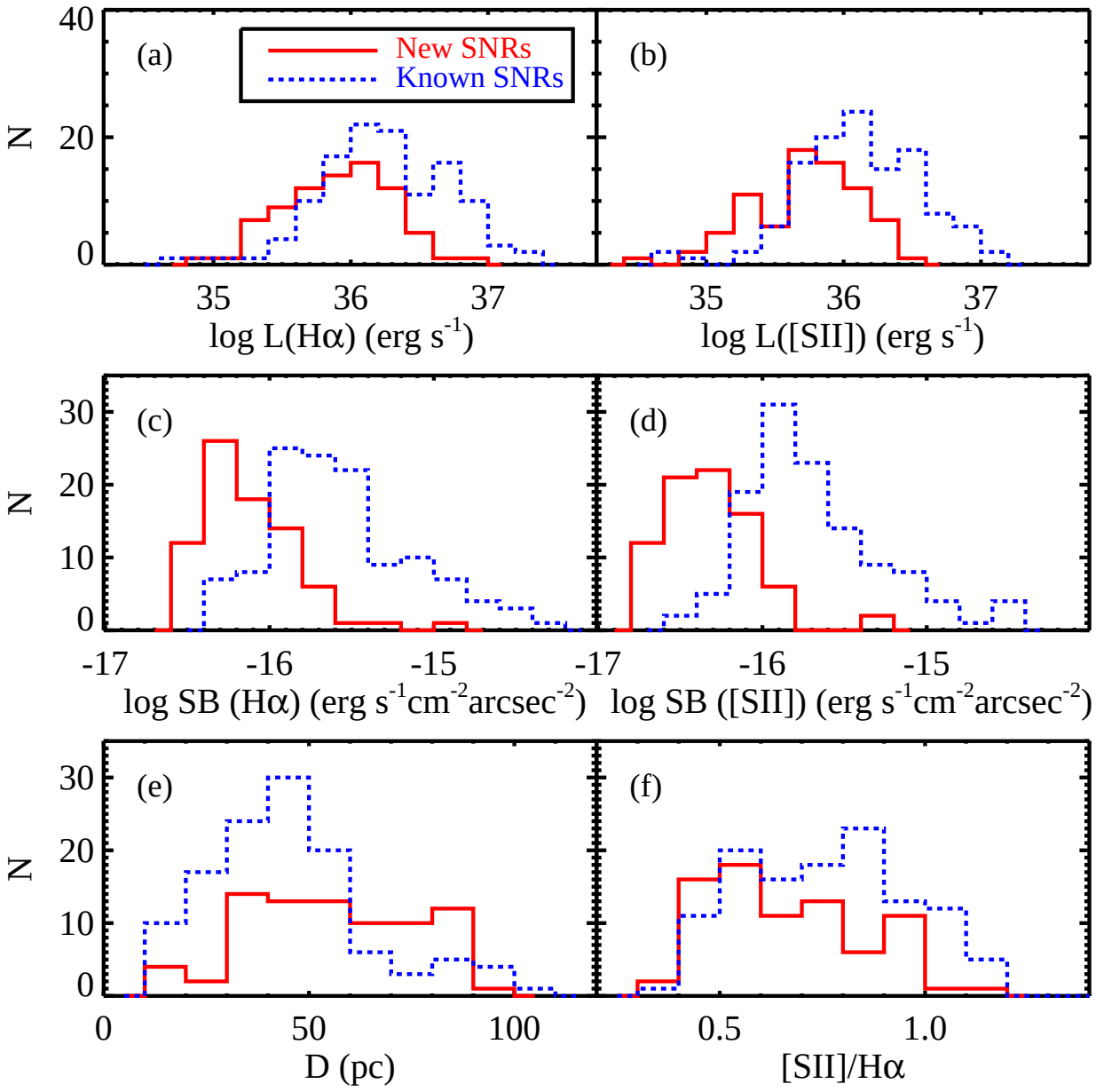

Fig. 12.— Comparisons of histograms of (a) L(Hα) and (b) L([S II]), (c) SB(Hα) and (d) SB([S II]), (e) D, and (f) [S II]/Hα of new remnants with those of known ones in M33.

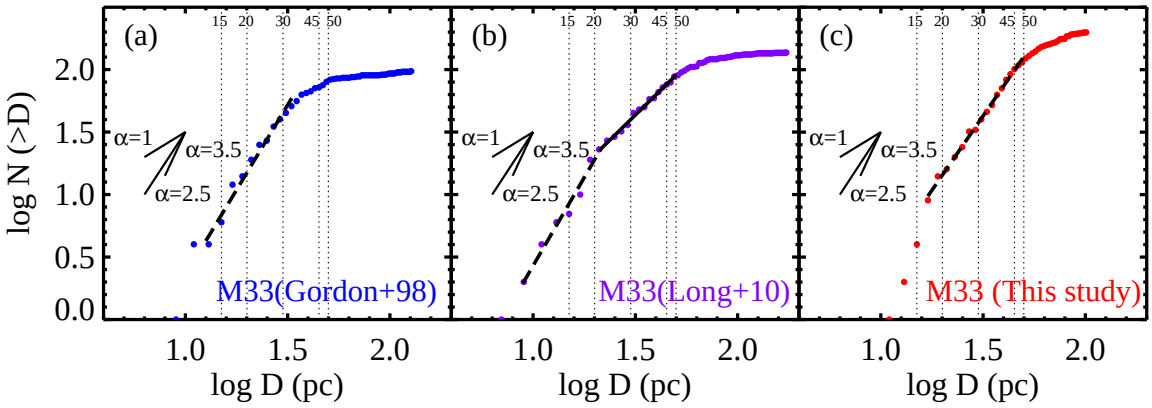

Fig. 13.— Comparison of cumulative size distributions of remnants in this work with those in the previous studies of M33: (a) G98, (b) L10, and (c) this work. Power law fits are represented by thick dashed lines.

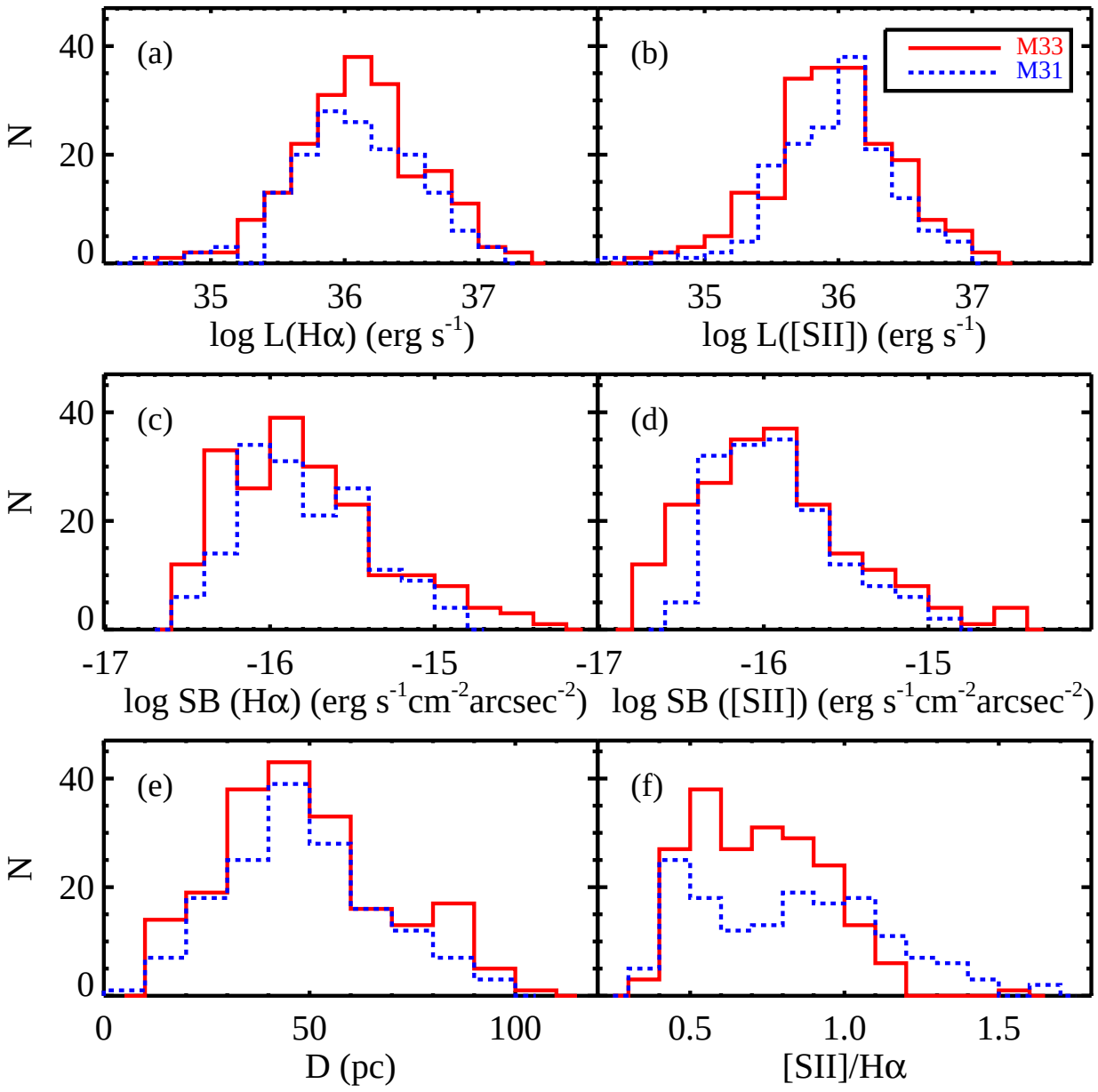

Fig. 14.— Comparisons of histograms of (a) L(Hα) and (b) L([S II]), (c) SB(Hα) and (d) SB([S II]), (e) D, and (f) [S II]/Hα of M33 remnants with those of M31 remnants (L14).

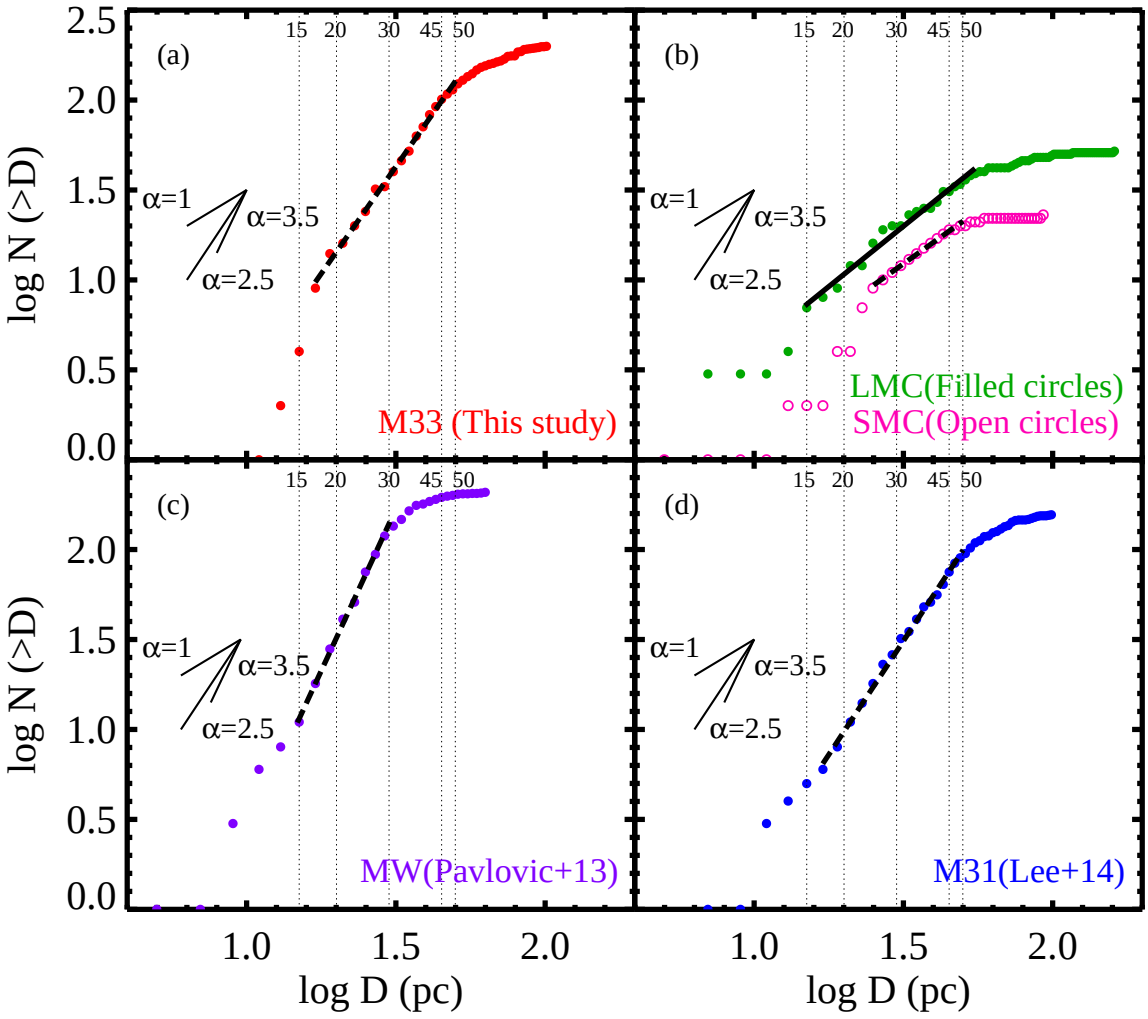

Fig. 15.— Cumulative size distributions of remnants in M33, the MCs, the MW, and M31. Samples for the MCs, the MW, and the M31 are obtained from B10, Pavlović et al. (2013), and L14, respectively. Power law fits are represented by thick lines. The power law indices for individual galaxies are summarized in Table 4.

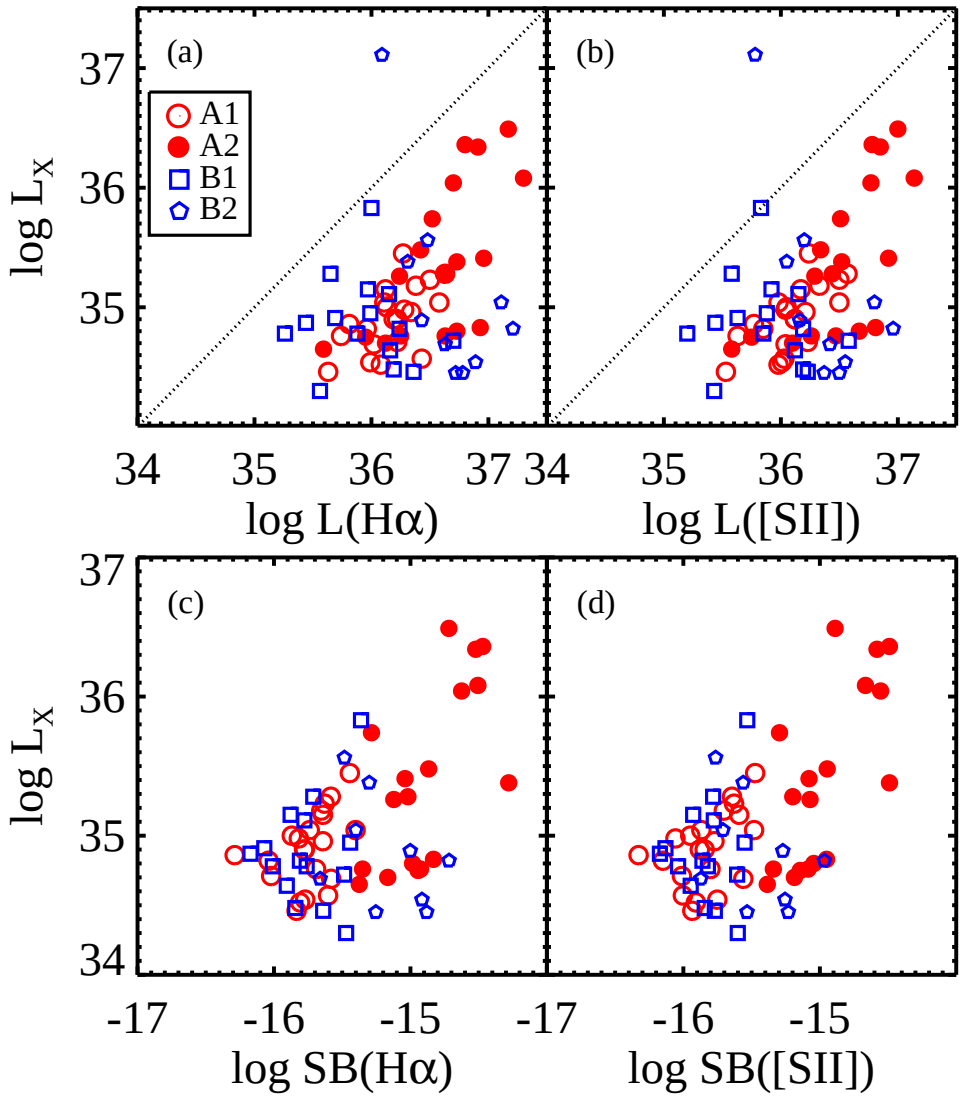

Fig. 16.— Comparisons of $L_{\rm X}$ and optical properties of remnants in this work and L10 for M33: (a) $L_{\rm X}$ versus L(Hα), (b) $L_{\rm X}$ versus L([S II]), (c) $L_{\rm X}$ versus SB(Hα), and (d) $L_{\rm X}$ versus SB([S II]).

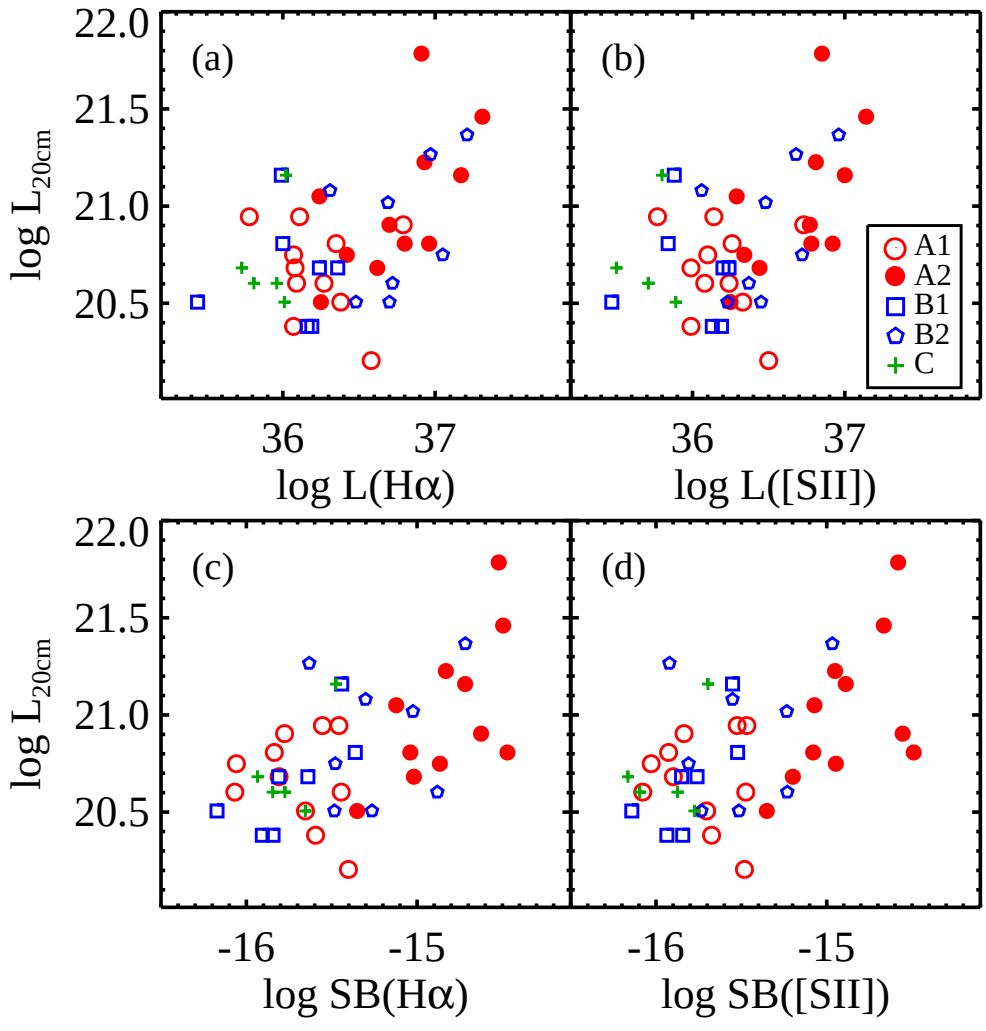

/

Fig. 17.— Comparisons of $L_{20\mathrm{cm}}$ and optical properties of remnants in this work and Gordon et al. (1999) for M33: (a) $L_{20\mathrm{cm}}$ versus $L(\mathrm{H}\alpha)$, (b) $L_{20\mathrm{cm}}$ versus $L([\mathrm{S\ II}])$, (c) $L_{20\mathrm{cm}}$ versus $SB(\mathrm{H}\alpha)$, and (d) $L_{20\mathrm{cm}}$ versus $SB([\mathrm{S\ II}])$.

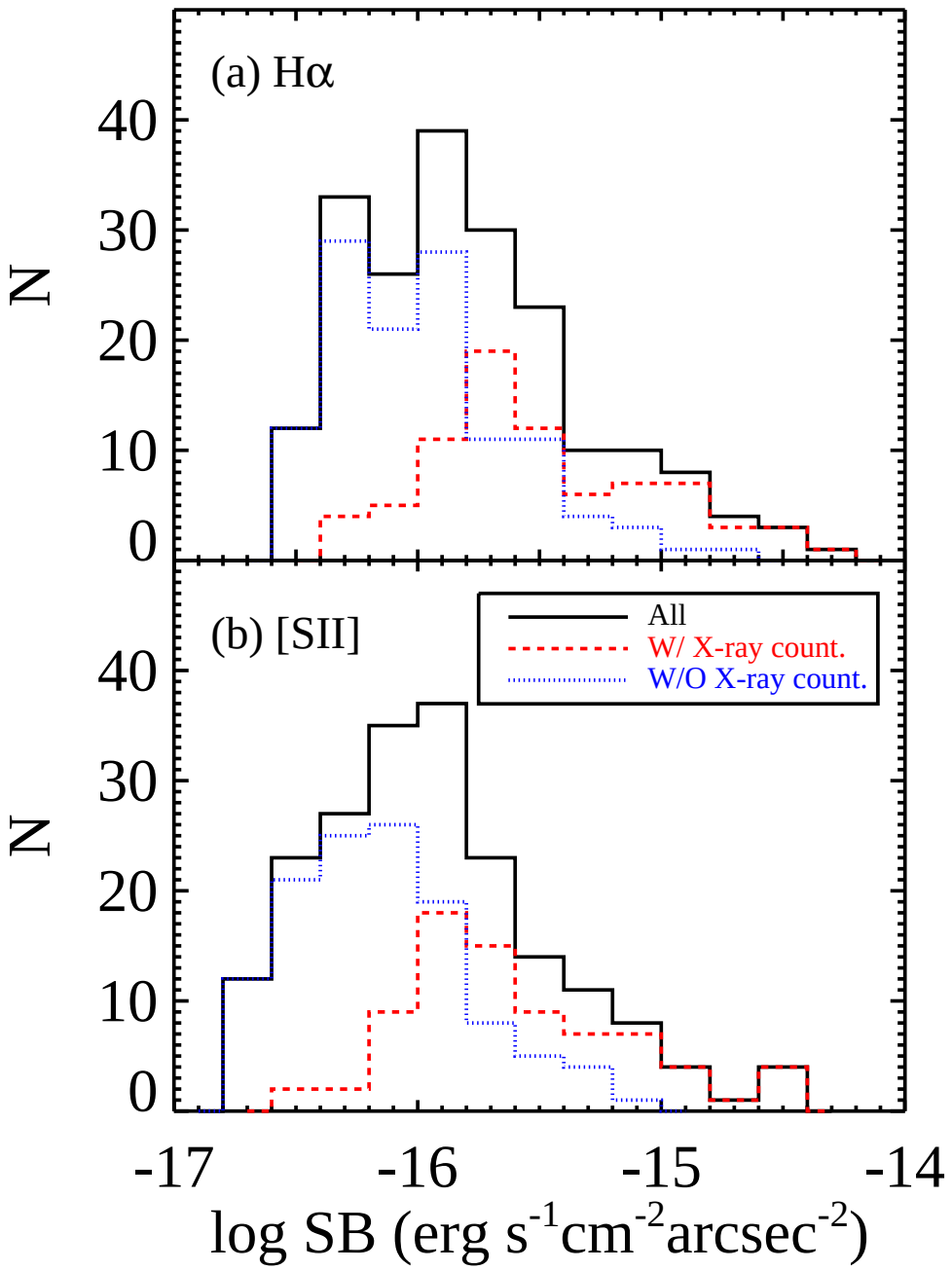

Fig. 18.— Histograms of (a) $SB(\mathrm{H}\alpha)$ and (b) $SB([\mathrm{S\ II}])$ of remnants with X-ray emission, those without X-ray emission, and all the M33 remnants.

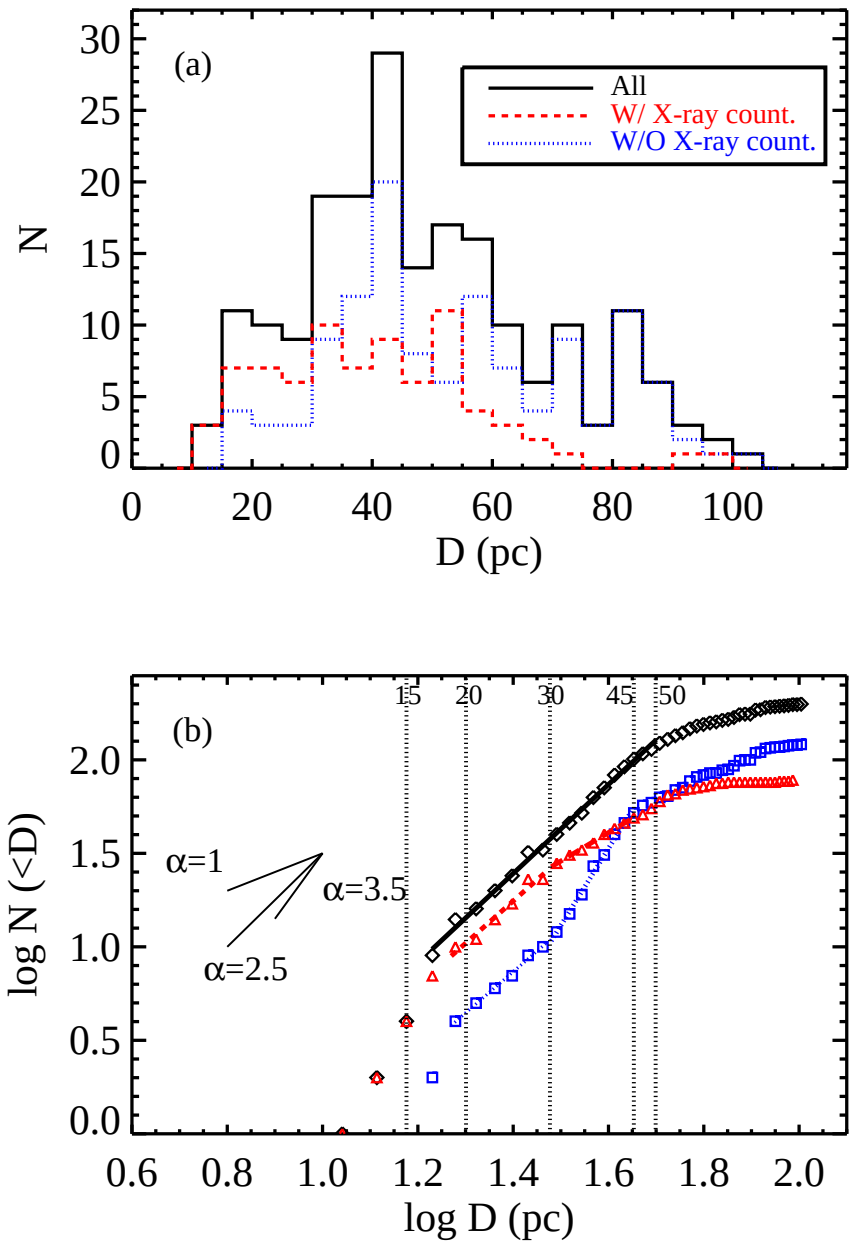

Fig. 19.— (a) Differential and (b) cumulative size distributions of remnants with X-ray emission, those without X-ray emission, and all the M33 remnants.